J Adv Ceram

Review

Advances in reactive air wetting and brazing of engineering ceramics

Mingfen Zhang[1], Shunjian Xu[2], Fabrizio Valenza[3], Xiangzhao Zhang[1], Guiwu Liu[1,✉], Guanjun Qiao[1,✉]

Cite this article: Zhang M, Xu S, Valenza F, et al. *J Adv Ceram* 2025, **14**(1): 9220997. https://doi.org/10.26599/JAC.2024.9220997

ABSTRACT: The reactive air brazing (RAB) process of ceramics was developed in the early 2000s because high-temperature electrochemical devices, such as solid oxide fuel cells (SOFCs), gas separators, reformers, and ion transport membrane systems, are increasingly emerging. Accordingly, the reactive air wetting (RAW) and RAB of oxide ceramics have been investigated. Starting from the introduction of the advantages of the RAB process, the thermal expansion coefficients (TECs) of related materials, and the estimation of the TECs of Ag-based composite fillers, the RAW and RAB of ceramics are reviewed by classifying the employed ceramic materials, which mainly include yttria-stabilized zirconia (YSZ), perovskite oxides, Al_2O_3, and nonoxide ceramics. In particular, the RAW and RAB processes, interfacial microstructures, reaction products, and joint reliability (including joint strength, fracture energy, gas tightness, and high-temperature aging resistance) are highlighted for understanding interfacial behavior and joint performance and developing application-oriented brazing technology. Finally, some helpful conclusions are drawn after summarizing the RAB of oxide ceramics. The prospects for RAB of SiC and high-entropy oxide ceramics are proposed after summarizing the RAB of oxide and nonoxide ceramics, and several aspects are proposed for promoting the development and application of RAB technology.

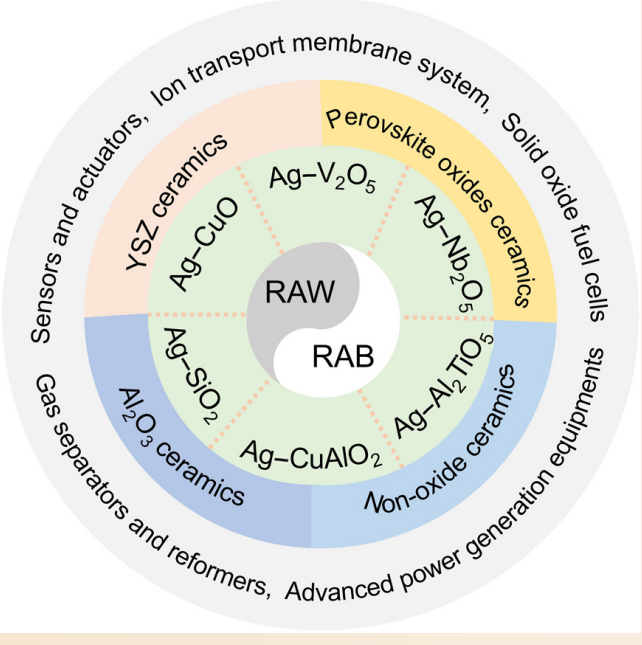

KEYWORDS: brazing; wetting; interfaces; microstructures; joint reliability

1 Introduction

High-temperature electrochemical devices, which include solid oxide fuel cells (SOFCs), ion transport membrane systems, and electrochemical gas separators and reformers, are currently widely used in many fields. The higher demands were put forward for brazed joints of functional ceramic materials due to special service environments (such as high temperature in oxidizing or reducing atmosphere, and dual atmosphere composed of air and fuel gases), where the functional ceramic materials involved are mainly yttria-stabilized zirconia (YSZ), alumina (Al_2O_3), and lanthanide, barium or lead perovskite-type oxides (i.e., mixed ionic/electronic conducting (MIEC) oxides), such as $La_{0.6}Sr_{0.4}Co_{0.2}Fe_{0.8}O_{3-\delta}$ (LSCF), $Ba_{0.5}Sr_{0.5}Co_{0.8}Fe_{0.2}O_{3-\delta}$ (BSCF), $Ba_{0.5}Sr_{0.5}(Co_{0.8}Fe_{0.2})_{1-x}Zr_xO_{3-\delta}$ (BSCFZ), $BaCo_{0.7}Fe_{0.2}Nb_{0.1}O_{3-\delta}$ (BCFN), $BaCo_{0.4}Fe_{0.4}Zr_{0.2}O_{3-\delta}$ (BCFZ), $BaZr_{0.1}Ce_{0.7}Y_{0.1}Yb_{0.1}O_{3-\delta}$ (BZCYYb) or conveniently doped $BaTiO_3$ (BTO), $BaZr_xTi_{1-x}O_3$ (BZT), and $PbZr_xTi_{1-x}O_3$ (PZT). Commonly, glass joining and active metal brazing (AMB) are suitable for bonding these oxide ceramics to metal components. Both techniques involve a filler that wets and adheres to the adjoining surfaces. However, the maximum operating temperature of a glass joint is limited by the lower softening point of the glass, the thermomechanical properties of the glass begin to deviate from the original state, and the devitrification of the glass occurs during service, resulting in the occurrence of additional complications [1]. Active metal brazing requires a high vacuum or protective atmosphere (reducing or inert gases), leading to operation complexity and inconvenience in actual industrial production to a certain extent, as well as possible modification of ceramic functional properties that are susceptible to oxygen partial pressure [2]. Moreover, the resulting brazed joints are unable to endure an oxidizing atmosphere at moderate

[1] School of Materials Science and Engineering, Jiangsu University, Zhenjiang 212013, China. [2] School of Intelligent Manufacturing, Huzhou College, Huzhou 313000, China. [3] National Research Council, Institute of Condensed Matter Chemistry and Technologies for Energy, CNR-ICMATE, Genoa 16149, Italy.

✉ Corresponding authors. E-mail: G. Liu, gwliu76@ujs.edu.cn; G. Qiao, gjqiao@ujs.edu.cn

Received: August 27, 2024; Revised: October 9, 2024; Accepted: October 31, 2024

to high temperatures. Thus, the reactive air brazing (RAB) process was developed in the early 2000s [3], which was actually derived from "direct copper bonding (DCB)". The RAB is conducted directly in air without the use of fluxing or reducing agents to promote wettability. The fillers are usually composed of noble metals (such as Ag, Pd, and Pt) whose oxides are not stable under the testing conditions and metal oxides (MO_x); the latter may be pure metals that undergo oxidation during the RAB process (e.g., Cu formed CuO). During brazing, the MO_x dissolved in a noble metal solvent is used to reactively modify the substrate surface, which makes the remaining molten filler wet the ceramic substrate well [4]. Moreover, compared with the use of inert gases or vacuum, the use of oxygen-containing atmospheres improves the wetting and adhesion of the liquid noble metal itself because of the oxygen adsorption at the interfaces. Consequently, the as-fabricated joints are relatively adherent, ductile, and intrinsically oxidation resistant.

In these high-temperature electrochemical devices, the functional ceramic components are usually joined with stainless steels (SSs) or high-temperature alloys. The mechanical and chemical reliability of joints must be considered in the service process. Indeed, the joint strength is closely related to the brazing process, interfacial behavior, and difference in TEC among the ceramics, metal components, and brazing filler. Table 1 lists the TECs of the related ceramics, metals, and constituents of RAB fillers [5–59]. From Table 1, the commonly employed YSZ, Al_2O_3, and zirconia-toughened alumina (ZTA) ceramics present moderately high TECs of ~(8–11)×10^{-6} K^{-1} [5–7,10–12], whereas the typical nonoxide ceramics (including Si_3N_4, AlN, and SiC) have quite lower TECs of (3–4.7)×10^{-6} K^{-1} [30–33]. The single-phase MIEC oxides (including LSCF, BSCF, BCFN, and BCFZ) have higher TECs of ~(17–20)×10^{-6} K^{-1}, except for the proton conductor (BZCYYb, ~10.3×10^{-6} K^{-1}) [14,17–25], whereas the dual-phase MIEC oxides (such as $Ce_{0.9}Gd_{0.1}O_{2-\delta}$–$La_{0.6}Sr_{0.4}Co_{0.2}Fe_{0.8}O_{3-\delta}$ (GDC–LSCF) and $Ce_{0.9}Gd_{0.1}O_{2-\delta}$–$La_{0.7}Sr_{0.3}MnO_{3\pm\delta}$ (GDC–LSM)) have lower TECs of ~13×10^{-6} K^{-1} due to the addition of GDC (or gadolinium-doped cerium oxide (CGO), ceria-gadolinia), with a TEC of ~12×10^{-6} K^{-1} [13–16]. The TECs (~6×10^{-6} and 1×10^{-6} K^{-1}) of BTO and PZT piezoelectric ceramics around room temperature (RT) are far lower than those

Table 1 TECs and/or melting points of related ceramics, metals, and brazing filler constituent

Brazing object				Brazing filler		
Ceramic	TEC (10^{-6} K^{-1})	Metal	TEC (10^{-6} K^{-1})	Constituents of brazing filler	Melting point (°C)	TEC (10^{-6} K^{-1})
YSZ	8.9–10.6 (RT) [5] 12 (RT–1000 °C) [6] 10.8 (20–1000 °C) [7]	Crofer 22 APU; X1CrTiLa22; (EN 1.4760)	11.8 (20–800 °C) [19] 12.7 (20–1000 °C) [11] 12.3 (RT–1000 °C) [6]	Ag	962	20 (20–800 °C) [19] 19.4 (20 °C); 21.7 (20–800 °C) [20] 18 (RT) [46]
NiO–YSZ	~12 (50–1000 °C) [8] 12.6 (20–1000 °C) [9]	Crofer 22 H (EN1.4755); X1CrWNbTiLa22-2	10.3 (20–200 °C) [20] 12 (20–900 °C) [20]	Au	1064	14.2 (RT) [12]
ZTA	8.35 (30–700 °C) [10]	AISI 442 (EN 1.4742); X10CrAlSi18	~13.5 (RT–1000 °C) [34]	Pd	1554	11.8 [47]
Al_2O_3	8.2 (20–1000 °C) [11] 7.8 (20 °C) [12]	AISI 441 (EN 1.4509); X2CrTiNb18	~11.9 (20–800 °C) [25] 12.1 (25–700 °C) [35]	Pt	1772	9 [48]
CGO (GDC)	~12.5 (25–1000 °C) [13] 11.9 (RT–800 °C) [14]	SUS 430 (EN 1.4016); AISI 430	12.44 (RT–850 °C) [36]	Al_2O_3	2054	6.5 (20–800 °C) [49]
GDC–LSCF	~13.2 (30–1000 °C) [15]	AISI 316 L (EN 1.4404) X2CrNiMo 17-12-2	20.86 (10–800 °C) [37] 21 (25–1200 °C) [38]	$CuAlO_2$	~2030	4.1 [50]
GDC–LSM	~12.7 (25–1000 °C) [16]	AISI 314 (EN 1.4841); X15CrNiSi25-21	18 (20–800 °C) [19] 19 (20–900 °C) [20] 15.7 (20 °C) [20]	Al_2TiO_5	1860	1–2 (20–1000 °C) [49] 1.4 (25–1000 °C) [51]
LSCF	16.3 (RT–425 °C) [14] 24.5 (425–1000 °C) [14] 20.6 (100–900 °C) [17] ~14 (RT) [18]	AISI 310S (EN 1.4845); X8CrNi25-21	14.4 (27–877 °C) [18] 19 (RT–1000 °C) [34]	TiO_2	1840	8.9 (RT) [52] 9.0 (RT) [53]
BSCF	18–22 (20–800 °C) [19] 19 (20–900 °C) [20] 14.7 (RT) [20]	17-4PH; AISI 630	14 (25–1000 °C, mean) [38] 11.0 (RT) [39]	SiO_2	1670	0.5 (25–1000 °C) [51]
BCFN	~18.2 (30–900 °C) [21]	Fecralloy	11.1 (27–877 °C) [40]	Nb_2O_5	1520	1.0 (25–1000 °C) [51] 0.54–1.79 (25–800 °C) [54]
BCFZ	14.4 (150–1000 °C) [22] 17 (RT–1000 °C) [23]	Kanthal APM; X8CrAl25-5	14.2 (20–800 °C) [19]	WO_3	1473	10 (20–800 °C) [55] ~12 (20–700 °C) [56]
BZCYYb	10.76 (30–800 °C) [24] ~9.9 (20–800 °C) [25]	FeCrAlY	~14 [41]	$LiAlSiO_4$	1417	−6.2 (25–1000 °C) [51]
BTO	~6 (RT) [26] ~10–13 (cubic, > T_c) [26,27]	GH3536	~12.1 (20–100 °C) [42] ~13 (RT) [43]	CuO	1326	9.3 (RT) [46] 4.3 (monoclinic, 70–650 °C) [57] 11.5 (27–800 °C) [58]
PZT	~1 (RT); ~10 (cubic, 650 °C) [28] 3.45 (20–110 °C, mean) [29]	Inconel 600	15.8 (27–877 °C) [18,40]	PbO	886	9.4 (tetragonal, 50–480 °C) [57] 3.3 (orthorhombic, 500–700 °C) [57]
SiC	4–4.7 (RT) [30–32]	Haynes 214	16.6 (20–800 °C) [19]	MoO_3	795	17.99 [59]
AlN	4.5 (RT) [33]	Ti6Al4V	8.4–9.5 (RT) [39,44,45]	V_2O_5	690	20.3 (RT–500 °C) [53]
Si_3N_4	3 [31]	—	—	—	—	—

~10×10^{-6} K^{-1} of the cubic phase over the Curie temperature (T_c) or at high temperatures, respectively [26–28]. Moreover, the TECs of ferrite SS (such as Crofer 22 APU, Crofer 22 H, AISI 442, AISI 441, and AISI 430) range from ~10.5×10^{-6} to 12.5×10^{-6} K^{-1} [6,11,19,20,25,34–36], whereas most austenite SS (such as AISI 316 L, AISI 314, and AISI 310S) have higher TECs of (15–21)×10^{-6} K^{-1} [18–20,34,37,38], and the TEC of 17-4PH martensite SS is between those of ferrite and austenite SS [38,39]. Ni-based high-temperature alloys (Inconel 600 and Haynes 214, ~16×10^{-6} K^{-1}) present higher TECs than do Fe–Cr–Al (Fecralloy, Kanthal APM, and FeCrAlY) and Fe–Ni–Cr (GH3536) alloys (~(11–14)×10^{-6} K^{-1}) [18,19,40–43] and Ti6Al4V (~9×10^{-6} K^{-1} at RT) [39,44,45]. Notably, the NiO–YSZ composite has a comparable TEC with the YSZ ceramics and ferrite SS [8,9], which makes them suitable for an anode support layer for SOFCs.

Possible noble metals in RAB fillers include Ag, Au, Pd, and Pt, which have decreasing TECs ((from ~19, 14, 12 to 9)×10^{-6} K^{-1}) and increasing melting points (from 962, 1064, 1554, to 1772 °C) [12,19,20,46–48]. Therefore, it is very inappropriate to employ Pd and Pt as host materials for RAB fillers because of their relatively high melting points; otherwise, the employed ceramics and metal components can be damaged in such a high-temperature air environment. The latter three noble metals (Au, Pd, and Pt) are quite expensive; thus, Ag was selected as the predominant noble metal. However, the room-temperature TEC of Ag is much greater than that of common ceramic components (Table 1) [5–32], resulting in considerable residual thermal stress at the interface and lower joint strength. The addition of most MO_x (or oxides) into Ag can effectively reduce TEC of the filler, especially for low-expansion $CuAlO_2$ [50], Al_2TiO_5 [49,51], SiO_2 [51], Nb_2O_5 [51,54], and $LiAlSiO_4$ [51]. For binary Ag-based composite fillers (where no chemical reaction occurs between Ag and the metal oxides), their TECs can be deduced via Eq. (1) [60]:

$$\alpha_{c1} = \alpha_{Ag}(1 - \phi_p) + \alpha_p\phi_p \quad (1)$$

where α_{c1}, α_{Ag}, and α_p are the TECs of the binary Ag-based composite filler, Ag, and metal oxide particle, respectively, and ϕ_p is the volume fraction of the metal oxide particle. In particular, TECs of Ag–CuO systems (such as Ag–2CuO, Ag–4CuO, and Ag–8CuO) can be estimated or determined experimentally at different temperatures [9,49,61]. Thus, for a ternary Ag–CuO–X system, the TEC can be calculated via Eq. (2) [62]:

$$\alpha_{c2} = \alpha_{Ag-CuO}(1 - \phi_p) + \alpha_p\phi_p \quad (2)$$

where α_{c2} and α_{Ag-CuO} are the TECs of the ternary Ag-based composite filler and Ag–CuO, respectively. As a result, TECs of Ag-based RAB fillers could be modulated by adding different volume fractions of metal oxide particles with various TECs to a certain extent. Two cases are that TECs of the Ag–2CuO–Al_2O_3 [62] and Ag–8CuO–Al_2TiO_5 [63] composite filler systems can be estimated after calculating the volume fractions of Al_2O_3 and Al_2TiO_5.

In addition to the simplicity and convenience of the RAB process, the greater advantage of RAB lies in the good service performance of the resulting joints at higher temperatures in air or oxidizing the atmosphere, which mainly depends on the employed noble metals and oxide particles. Some RAB joints can serve in a wet oxidizing atmosphere or dry or wet reducing atmosphere. Therefore, the service reliability of RAB joints under different environments is crucial for their practical applications. To motivate the RAB process and expand the application of RAB joints, we review the reactive air wetting (RAW) and RAB of ceramics by classifying the employed ceramic components, including functional ceramic components (YSZ, CGO, and perovskite oxide ceramics) and structural ceramic components (Al_2O_3 and nonoxide ceramics). The wetting and joining processes, interfacial microstructures and/or reaction products, as well as joint strength, leakage rate, and fracture energy before and after high-temperature aging in different atmospheres, are highlighted for optimizing the RAB process, understanding the interfacial behavior and joint reliability, and supporting the development of application-oriented RAB techniques.

2 Functional ceramic components

Currently, SOFCs can be divided into planar, tubular, flat-tubular, and monolithic types in accordance with the cell design, which is composed mainly of an anode (fuel electrode), an electrolyte, a cathode (air electrode), and an interconnect or bipolar separator. SOFCs are usually divided into anode-supported (AS), electrolyte-supported (ES), cathode-supported (CS), inert substrate-supported (SS), and metal-supported (MS) types according to their supporting components [64]. In particular, a planar anode-supported SOFC consists of a NiO–YSZ support layer, a thin NiO–YSZ active anode layer, a dense YSZ electrolyte layer, a porous CGO barrier layer, and a perovskite-type cathode [60]. Therefore, the sealing of SOFCs mainly involves the RAW and RAB of YSZ, NiO–YSZ, CGO, and perovskite oxides to themselves or SS or high-temperature alloys.

2.1 YSZ

2.1.1 RAW of YSZ

On the basis of the CuO–Ag binary phase diagram (Fig. 1), possible braze compositions with Ag contents of 30.65–98.60 mol% could be developed from the two invariant points (monotectic reaction and eutectic reaction points at 964±3 and 932±3 °C, respectively) [1,65]. Therefore, Ag–CuO or Ag–Cu brazing fillers with CuO or Cu contents of 1–69 mol% are often used to perform RAW and RAB of ceramics. At temperatures of 1000–1150 °C, the apparent contact angle of Ag on YSZ decreased under an air atmosphere compared with an inert atmosphere or vacuum, and Ag–CuO or Ag–Cu on YSZ decreased from 90°–130° to ~30° and to less than 10°, with the CuO or Cu content increasing from

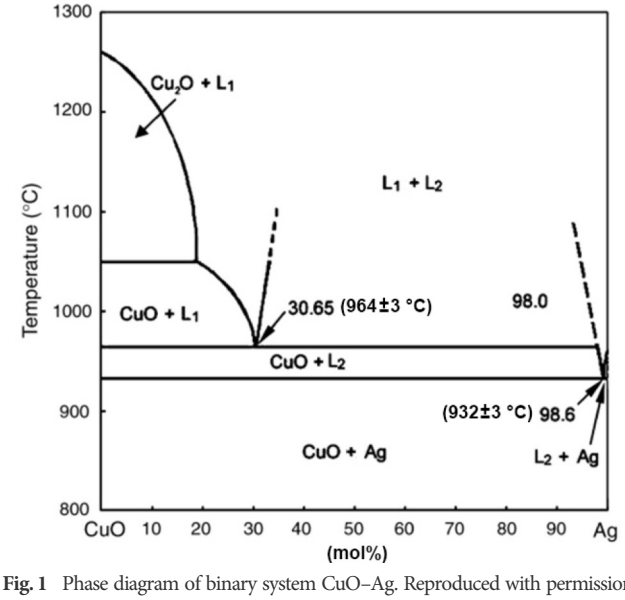

Fig. 1 Phase diagram of binary system CuO–Ag. Reproduced with permission from Ref. [1], © The American Ceramic Society 2005.

0%–8% and to over 40 mol% (Table 2) [66–72], which can be attributed mainly to the formation of Ag-dissolved O clusters adsorbed at the Ag/YSZ interface and CuO interlayers between Ag and YSZ (Fig. 2) [73]. The addition of small amounts of TiO_2 (derived from the decomposition and oxidation of TiH_2) into the Ag–CuO system can lower the contact angle, which can be ascribed mainly to the interfacial interaction between YSZ and TiO_2 [67,68]. However, the addition of Al_2O_3 or Pd results in an increase in the contact angle [71,74]. The addition of Al_2O_3 can reduce the role of CuO by hindering the flow of the CuO-rich liquid phase toward the YSZ/braze interface and consuming the CuO-rich liquid phase due to the formation of the $CuAl_2O_4$ phase [71]. Similar to the Ag–CuO/YSZ system, the addition of V_2O_5 to Ag can greatly lower the contact angle of the Ag/YSZ system [69]. Moreover, the addition of a certain amount of $CuAlO_2$ or SiO_2 to Ag can lead to a substantial increase in the wettability of Ag/YSZ systems, with a final contact angle of ~40°–50° [75,76]. Generally, noble metals (Ag and Pd) and oxides (such as CuO, V_2O_5, Al_2O_3, $CuAlO_2$, and SiO_2) cannot react with the YSZ substrate during wetting. However, TiO_2 (derived from TiH_2) can react with ZrO_2 to form titanium zirconate along the braze/YSZ interface [67]. Therefore, it can be concluded that the Ag–CuO (or Ag–Cu), Ag–$CuAlO_2$, and Ag–V_2O_5 systems can effectively wet YSZ, whereas the Ag–SiO_2 and Ag–Al systems present relatively poor wettability of YSZ. In particular, the addition of a third component (such as TiO_2, Al_2O_3, or Pd) to Ag–CuO can cause certain changes in the contact angle, which mainly depends on the added content. Therefore, Ag–CuO and Ag–$CuAlO_2$ seem to be two promising RAB fillers for YSZ because of their wettability and high-temperature resistance.

2.1.2 *RAB of YSZ*

Generally, good wettability signifies high interfacial bonding and high joint strength. However, the highest joint strength is not often derived from the lowest contact angle. Table 3 summarizes the joining processes, joint stability, and main interfacial products for RAB of YSZ ceramics [6,9,20,62,63,66–72,74–94]. As shown in Table 3, the filler systems employed in RAB of YSZ include Ag [81–86], Al [91], Ag–Al [20,68,85,86], Ag–Cu [6,20,68,77,81,83–86], Ag–CuO [66,67,69–71,78,87,88,90,92], Ag–V_2O_5 [69], Ag–Al_2TiO_5 [9], Ag–SiO_2 [76,89], Ag–$CuAlO_2$ [75], and Ag–Nb_2O_5 [95], and Ag–CuO (or Ag–Cu) system also includes third components, such as Ti [68], TiH_2 [67,78,88], Pd [74,79,80], Al_2O_3 [62,71], and Al_2TiO_5 [63,94]. The brazing temperature depended mainly on the employed oxides, the added third components, and their contents. For example, the brazing temperature of the Ag–Cu or Ag–CuO filler was mainly 1000 or 1050 °C, whereas it was increased to 1100–1150 °C after the addition of a certain amount of Pd, Al_2O_3, and Al_2TiO_5, which have relatively high melting points. The higher brazing temperatures were mainly set as 1120–1200 °C for the Ag–SiO_2, Ag–$CuAlO_2$, and Ag–Nb_2O_5 systems. On the basis of the actual applications, the objects joined with the ZrO_2 ceramics involved Crofer 22 APU, Crofer 22 H, FeCrAlY, Fecralloy, AISI 314, AISI 441, AISI 310S, GH3536, Cocoated AISI 441, $(Mn,Co)_3O_4$-coated Crofer 22 APU, and Al-coated Crofer 22 H in addition to themselves (Table 3).

The joint strength, leakage rate, and fracture energy of the YSZ/YSZ and YSZ/metal joints were characterized in terms of joint performance before and after aging in oxidizing and/or reducing atmospheres, where the joint strength was measured by

Table 2 RAW of YSZ ceramics: wetting process and contact angle

Substrate	Drop material	Wetting condition	Minimum contact angle (°)	Ref.
5YSZ	Ag-1-69CuO	1050 °C × 15 min	< 10	[66]
8YSZ	Ag-1-8CuO Ag-1-8CuO-0.5TiH_2	(1000–1100) °C × 15 min	30.6 27.2	[67]
3YSZ	Ag-8Cu Ag-8Cu-0.5Ti Ag-0.5Al	1150 °C × 20 min	37 30 40	[68]
3Mg-PSZ	Ag-1-10 wt% CuO Ag-1-10 wt% V_2O_5	(1000–1100) °C × (15–60) min	~19 ~23	[69]
3Y-TZP	Ag-1-10 wt% CuO Ag-1-10 wt% V_2O_5	(1000–1100) °C × (15–60) min	~14 ~32	[69]
3YSZ	Ag-1-80CuO	1050 °C × 30 min	20	[70]
3YSZ 3YSZ Cu-3YSZ	Ag-8CuO Ag-8CuO-8 wt% Al_2O_3 Ag-8CuO-8 wt% Al_2O_3	1050 °C × 30 min	31 60 38	[71]
YSZ	Ag-0-40Cu	1050 °C × 30 min	~0	[72]
8YSZ	$Ag_{0.85}Pd_{0.15}$-0-69Cu	(1150–1250) °C × 10 min	~18	[74]
3YSZ	Ag-0.2-8 wt% $CuAlO_2$	1000 °C × 30 min	~38±2	[75]
YSZ	Ag-0-1 wt% SiO_2	1000 °C × 30 min	50±2	[76]

Note: All the concentrations of oxides in brazing fillers are in mol% throughout the whole text except the marked wt%.

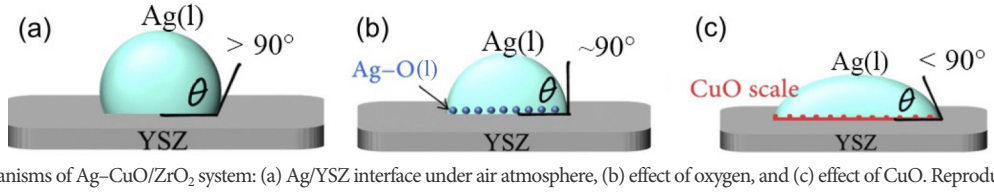

Fig. 2 RAW mechanisms of Ag–CuO/ZrO_2 system: (a) Ag/YSZ interface under air atmosphere, (b) effect of oxygen, and (c) effect of CuO. Reproduced with permission from Ref. [73], © Acta Materialia Inc. 2018.

Table 3 RAB of YSZ ceramics: joining process, joint performance, and interfacial products

Joining system	Brazing filler	Brazing condition	Joint performance	Maximum average strength; leak rate; fracture energy	Interfacial product	Ref
5YSZ/Crofer 22 APU	Ag-4Cu	1000 °C × 15 min	Rupture strength	~130 psi, 750 °C × (200-800) h, dry flowing air-aged or wet H_2-aged (RT-75) °C × 75 °C·min^{-1} × (5-50) cycles, dry flowing air or dry Ar + 2.75%H_2	—	[77]
5YSZ/FeCrAlY	Ag-1-69CuO	1050 °C × 30 min	Rupture strength	~114 psi, 750 °C × (500-800) h, air or wet H_2-aged ~112 psi, (750-70) °C × (5-40) cycles in air	$CuAlO_2$	[66]
8YSZ/8YSZ	Ag-1-8CuO Ag-1-8CuO-0.5TiH_2	1000 °C × 60 min × 5 kPa	4PB strength (rectangular)	111 MPa ~127 MPa	Ti zirconate	[67]
3YSZ/3YSZ 3YSZ/X1CrTiLa22 8YSZ/X1CrTiLa22	Ag-8Cu Ag-8Cu-0.5Ti Ag-0.5Al	1150 °C × 20 min	Microhardness	—	Zr-Ti mixed oxide layer, (Fe,Cr,Cu)O, and (Fe,Cr,Cu,Ti)O	[68]
8YSZ/fecralloy/8YSZ	Ag-1-8CuO; Ag-1-8CuO-0.5TiH_2	1000 °C × 60 min	4PB strength (double joint, rectangular)	101 MPa	$CuAlO_2$	[78]
8YSZ/8YSZ	$Ag_{0.85}Pd_{0.15}$-0-69Cu	1150 °C × 30 min	4PB strength (rectangular)	~98 MPa	—	[74]
YSZ/YSZ	Ag-1-64CuO-(0,5,15)Pd	1000 °C × 60 min	4PB strength (rectangular)	148 MPa	—	[79]
YSZ/YSZ	Ag-1-16CuO-(0,15)Pd	1100 °C × 15 min	4PB strength (rectangular)	148 MPa; 121 MPa (600 °C) 80 MPa (800 °C)	—	[80]
Crofer 22 APU/TZ3Y/Crofer 22 APU	Ag Ag-8Cu	1000 °C × 5 min × 1.5 MPa	Shear strength (DLO)	19.3/4.3 MPa (550/800 °C) 21.3/5.5 MPa (550/800 °C)	—	[81]
Crofer 22 APU/8YSZ/Crofer 22 APU	Ag	1000 °C × 5 min × 1.5 MPa	Shear strength (DLO)	11.6 MPa (550 °C) 3.9 MPa (800 °C)	—	[82]
Crofer 22 APU/TZ3Y/Crofer 22 APU	Ag Ag-8Cu	1000 °C × 5 min × 1.5 MPa	Fracture energy (4PB, notched multilayer)	> 300 J·m^{-2} 144±23 J·m^{-2}	Cu/Cr/Mn/Fe-oxide	[83]
Crofer 22 APU/TZ3Y/Crofer 22 APU	Ag Ag-8Cu	1000 °C × 5 min × 1.5 MPa	Fracture energy (4PB, notched multilayer)	271±29 J·m^{-2} 139±27 J·m^{-2}, 800 °C × 500 h, air-aged 134±20 J·m^{-2} 43±7 J·m^{-2}, 800 °C × 500 h, Ar-4H_2-1H_2O-aged	—	[84]
Crofer 22 H/TZ3Y/Crofer 2 2H CroFer 22 APU/TZ3Y/CroFer 22 APU	Ag, Ag-4Cu Ag-8Cu Ag-0.5Al, Ag Ag-8Cu	1000 °C × 5 min × 1.5 MPa	Fracture energy (4PB, notched multilayer)	> 253 J·m^{-2} > 253 J·m^{-2} 129±39 J·m^{-2} > 253 J·m^{-2} > 300 J·m^{-2} 144±23 J·m^{-2}	—	[85]
Crofer 22 H/TZ3Y/Crofer 22 H	Ag Ag-4Cu Ag-0.5Al	1000 °C × 5 min × 1.5 MPa	Fracture energy (4PB, notched multilayer)	~140 J·m^{-2}, (800-200) °C × 375 cycles ~30 J·m^{-2}, (800-200) °C × 117 cycles >253 J·m^{-2}, (800-200) °C × 500 cycles	—	[86]
3YSZ/Crofer 22 APU	Ag-4CuO	1000 °C × 60 min; 1000/1050 °C × 0.5 min; 1050 °C × 5 min	He leak rate	4.9×10^{-9} mbar·L·s^{-1}·cm^{-1} 2.6×10^{-11} mbar·L·s^{-1}·cm^{-1}	—	[87]
3YSZ/Crofer 22 APU	Ag-4 wt% Cu (Cu/Ag/Cu)	(1000-1100) °C × 5, 30 min	Shear strength (SL)	101±4 MPa	—	[6]
3Mg-PSZ/3Mg-PSZ; 3Y-TZP/3Y-TZP	Ag-1-10 wt% CuO Ag-1-10 wt% V_2O_5	(1000-1100) °C × (15-60) min	4PB strength (rectangular)	~255 MPa, ~180 MPa ~540 MPa, ~160 MPa	—	[69]
3YSZ/AISI 314	Ag-3Cu; Ag-0.5Al; Ag-2Fe-2Si-2Al	970 °C × 18 min 1050 °C × 18 min 1050 °C × 18 min	—	—	—	[20]
3YSZ/Crofer 22 APU	Ag-4CuO; Ag-4CuO-0.5TiH_2	1000 °C × 20 min	He leak rate	7×10^{-10} mbar·L·s^{-1}·cm^{-1} 5×10^{-11} mbar·L·s^{-1}·cm^{-1} ~5×10^{-11} mbar·L·s^{-1}·cm^{-1}, 850 °C × 800 h, air-aged 7×10^{-4} mbar L·s^{-1}·cm^{-1}, 850 °C × 800 h, 92.4N_2-4.6H_2-3H_2O-aged	—	[88]

(Continued)

Joining system	Brazing filler	Brazing condition	Joint performance	Maximum average strength; leak rate; fracture energy	Interfacial product	Ref
YSZ/Crofer 22 APU; NiO–YSZ/Crofer 22 APU	Ag; Ag-5-17.5 wt% Al_2TiO_5	(920-950) °C × 20 min × 320 kPa	H_2 leak rate	(0.02-0.225) sccm·cm^{-1} (0.2-0.9) sccm·cm^{-1} No severe degradation, 850 °C × 500 h, 50H_2O–45.5Ar–4.5H_2-aged Delamination, 850 °C × 500 h, O_2-aged	Ag_2CrO_4	[9]
Cu–3YSZ/Cu–3YSZ	Ag-8CuO-0-12 wt% Al_2O_3	1050 °C × 30 min × 1 kPa	Shear strength (SLO); He leak rate	60 MPa (3.2±0.9)×10^{-10} Pa·m^3·s^{-1}	—	[62]
3YSZ/3YSZ Cu–3YSZ/Cu–3YSZ	Ag-8CuO-8 wt% Al_2O_3	(1000-1150) °C × 30 min × 1 kPa	Shear strength (SLO)	40 MPa 24 MPa (800 °C), 62 Mpa 41 MPa (800 °C) 38 Mpa (800 °C × 150 h, air-oxidized)	$CuAlO_2$	[71]
3YSZ/Al_2O_3	Ag-1-80CuO	1050 °C × 30 min × 1 kPa	Shear strength (SLO) He leak rate	~45 MPa (2.9±0.9)×10^{-10} Pa·m^3·s^{-1}	$CuAl_2O_4$	[70]
8YSZ/8YSZ	Ag-0-4 wt% SiO_2	(960-1150) °C × 30 min × ~20 kPa	Shear strength (SLO)	47 MPa	—	[89]
YSZ/Co-AISI 441	Ag-0-1 wt% SiO_2	1000 °C × 30 min	—	—	Co_3O_4, Co_2SiO_4 $(Co,Fe)_3O_4$	[76]
8YSZ/AISI 441 8YSZ/Co-AISI 441	Ag-4CuO	960 °C × 30 min × 100 kPa	Shear strength (SLO)	33 MPa 51 MPa	Cr_2O_3, $(Co,Fe,Cu)_3O_4$	[90]
3YSZ/AISI 310S	Ag-0.2-8 wt% $CuAlO_2$	970-1120 °C × (5-90) min × 4.7 kPa	Shear strength (SLO)	93.7 MPa 50 MPa, 80 °C × 200 h, air-aged	$CuAl_2O_4$	[75]
YSZ/$(Mn,Co)_3O_4$-Crofer 22 APU	Ag-0-40Cu	1050 °C × 30 min × 1 kPa	Shear strength (SLO)	~55 MPa ~50 MPa, 800 °C × 200 h, air-aged	—	[72]
3YSZ/3YSZ	Al	(950-990) °C × 60 min	Shear strength (SLO)	~36 MPa	—	[91]
3YSZ/Al-Crofer 22 H	Ag-2-6CuO	(970-1100) °C × 30 min	Shear strength (SLO)	~44.3 MPa	$CuAl_2O_4$	[92]
YSZ/AISI 310S	Ag-0.3-25 wt% Nb_2O_5	(1130-1200) °C × (10-60) min	Shear strength (SLO)	110 MPa >40 MPa, 800 °C × 350 h, air-aged	$AgNbO_3$, $Nb_2Zr_6O_{17}$, and $CrNbO_4$–Cr_2O_3	[93]
5YSZ/5YSZ	Ag-8CuO-0-20 wt% Al_2TiO_5	(1020-1110) °C × (5-60) min	Shear strength (SLO)	104 MPa 100 MPa, 800 °C × (25-100) h, air-aged	$ZrTiO_4$	[63]
5YSZ/GH3536	Ag-8CuO-10 wt% Al_2TiO_5	1050 °C × 30 min	Shear strength (SLO)	62 MPa ~20 MPa, 800 °C × (50-1000) h, air-aged	$ZrTiO_4$, $NiAl_2O_4$, $NiCuO_2$, and $(Ni,Fe,Cr)_3O_4$–Cr_2O_3	[94]

Note: 1 sccm·cm^{-1} = 1.69×10^{-2} mbar·L·s^{-1}·cm^{-1} = 1.69×10^{-3} Pa·m^3·s^{-1} ·cm^{-1}.

4-point bending (4PB), single lap (SL), single lap offset (SLO), and double lap offset (DLO) shear modes. As indicated in the review article [95], ceramic/ceramic or ceramic/metal joints can be characterized mainly by shear, flexural/bending, and tensile strength, and the similarities and differences are discussed fully, accompanied by shear strength evaluation methods (including the SL, SLO, and DLO shear modes) and partial joint configurations. For the RAB joints of the ceramics, the 4PB mode involved rectangular (including single and double joints), round, and notched multilayer samples. In particular, a notched multilayer sample is used to characterize the interfacial fracture energy of a joint on the basis of the generation of a crack, which propagates from a notch tip along the interface in bending mode [83]. Indeed, the maximum 4PB strengths of rectangular YSZ/YSZ joints and the maximum shear strength of YSZ/YSZ joints were greater than 100 MPa when Ag-CuO-based [67,78–80] and Ag-V_2O_5 [69] fillers were employed, whereas the YSZ/YSZ joint strength was lower than 50 MPa when Ag-SiO_2 and Al were used as brazing fillers [89,91]. The addition of TiH_2, Pd, Al_2O_3, or Al_2TiO_5 to the Ag-CuO system can cause more or less variation in the YSZ/YSZ joint strength (Table 3). Generally, the SLO shear strength of YSZ/SS joints fluctuates in the range of 30-90 MPa [62,72,75,90,92,94]. However, the maximum shear strength of the YSZ/Ag-Nb_2O_5/AISI 310 s joint reached 110 MPa, mainly because of the formation of $AgNbO_3$ between Ag and Nb_2O_5 (Fig. 3(a)), which enables the wetting and bonding of YSZ/Ag–Nb_2O_5 interface [93]. Moreover, the greater addition of Nb_2O_5 and longer holding time can facilitate the reactive formation of the $Nb_2Zr_6O_{17}$ phase between ZrO_2 and Nb_2O_5, which can cause severe dissolution of YSZ and residual voids at the interface, thus reducing the joint strength and long-term stability [93]. The addition of TiH_2 and Al_2TiO_5 in the Ag-CuO

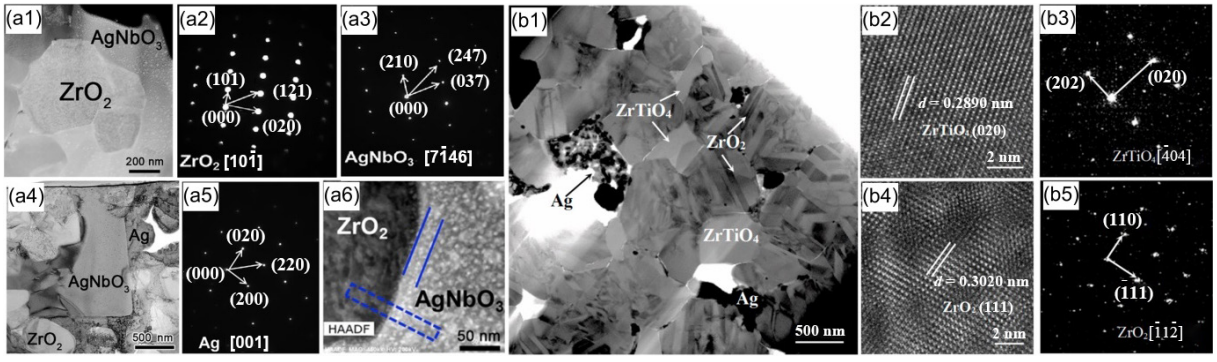

Fig. 3 (a1–a6) TEM images near Ag–Nb_2O_5/ZrO_2 interface and corresponding SAED patterns, indicating formation of $AgNbO_3$ and $AgNbO_3$/ZrO_2 interfaces; (b1–b5) TEM images near Ag–8CuO–10 wt% Al_2TiO_5/ZrO_2 interface and corresponding SAED patterns, indicating formation of $ZrTiO_4$. Reproduced with permission from Ref. [93] for (a1–a6), © Elsevier Ltd and Techna Group S.r.l. 2019; Ref. [63] for (b1–b5), © Elsevier Ltd and Techna Group S.r.l. 2021.

system can cause the formation of Ti zirconate ($ZrTiO_4$ phase) via the reaction between ZrO_2 and TiO_2 at the ceramic/interlayer interface (Fig. 3(b)) [63,67], which can increase the joint strength by ~15% and 110%, respectively, due to the alleviation of residual stress.

Kuhn [83–86] reported that the fracture energy of a YSZ/Ag/SS joint (notched multilayer specimen) was greater than 300 $J{\cdot}m^{-2}$ for Crofer 22 APU or 253 $J{\cdot}m^{-2}$ for Crofer 22 H. The fracture energy of the YSZ/Ag/SS and YSZ/Ag–Cu/SS joints decreased significantly after thermal cycle aging or isothermal aging in an oxidizing or reducing atmosphere, especially the fracture energy of the YSZ/Ag–8Cu/SS joint, which decreased by ~50%, but that of the YSZ/Ag–Al/SS joint was hardly reduced before and after thermal cycle aging in air. The He leak rates of as-brazed YSZ/SS, YSZ/YSZ, and YSZ/Al_2O_3 joints lay in the order of magnitudes of 10^{-9}–10^{-11} $mbar{\cdot}L{\cdot}s^{-1}{\cdot}cm^{-1}$ while employing Ag–CuO based fillers [62,70,88], and that of YSZ/Crofer 22 APU joint can stay on the order of magnitude of 10^{-9}–10^{-11} $mbar{\cdot}L{\cdot}s^{-1}{\cdot}cm^{-1}$ after high-temperature aging in air, while it decreased sharply to the order of magnitude of 10^{-4} $mbar{\cdot}L{\cdot}s^{-1}{\cdot}cm^{-1}$ and even to an unmeasurable level after the isothermal aging at 850 °C × 800 h in the dual atmospheres (92.4N_2–4.6H_2–3H_2O) (Fig. 4) [88]. This occurred because CuO can be reduced into elemental Cu due to the presence of H_2, resulting in the generation of voids near the interface and a sharp decrease in the gas-tightness and strength of the joint [4,96]. Alternatively, no severe degradation occurred in the NiO–YSZ/Ag–Al_2TiO_5/Crofer 22 APU joint after isothermal aging at 850 °C × 500 h in a reducing atmosphere (50H_2O–45.5Ar–4.5H_2), whereas delamination between the steel and the braze was produced after isothermal aging in pure oxygen [9].

In addition, during RAB, CuO can react with Al_2O_3 to form $CuAlO_2$ or $CuAl_2O_4$ at the interface (where the Al_2O_3 originates from the oxidization of metal components or the addition into brazing filler) [66,70,71,75,78,92], and other compositions of brazing fillers (such as Ag, SiO_2, Nb_2O_5, and Al_2O_3 from the decomposition of Al_2TiO_5) can also react with the compositions of metal components to form Ag_2CrO_4 [9], Co_2SiO_4 [76], $CrNbO_4$ [93], and $NiAl_2O_4$ [63]. Notably, CuO can also easily react with steels in air at high temperatures, forming dense and thick Fe/Cr/Cu/Mn(Ti,Ni)-oxide reaction layers at the braze/interconnect interface, thus decreasing joint reliability [18,68,83,94]. As a result, some coatings (such as Co, Al, and $(Mn,Co)_3O_4$) have been developed on metal components [72,76,90,92].

In short, Ag–CuO (–TiO_2 or Al_2TiO_5), Ag–Nb_2O_5, and Ag–$CuAlO_2$ systems are better RAB fillers for YSZ in terms of the strength of YSZ/YSZ or YSZ/SS joints. However, severe

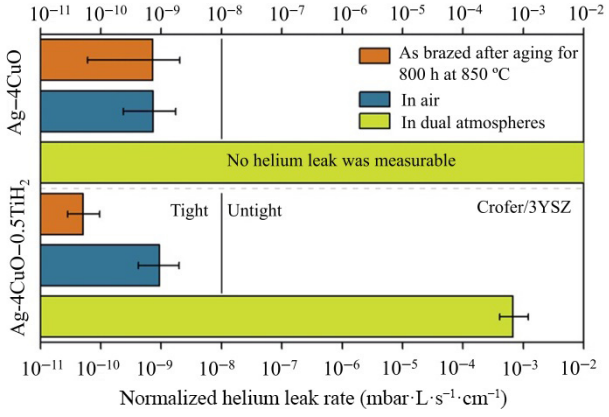

Fig. 4 Gas-tightness of 3YSZ/Crofer 22 APU RAB joints before and after aging in air and in dual atmospheres. Reproduced with permission from Ref. [88], © WILEY-VCH Verlag GmbH & Co. KGaA, Weinheim 2015.

degradation of the He leakage rate of the Ag–CuO-based joints can be produced after high-temperature isothermal aging in a reducing atmosphere, and obvious degradation in the joint strength can occur in the YSZ/SS joints after isothermal aging in air. Therefore, the Ag–CuO (only applied in an oxidizing atmosphere), Ag–Nb_2O_5-, and Ag–$CuAlO_2$-based systems are the three promising RAB fillers for YSZ, and it is necessary to apply an oxidation-resistant coating on the SS.

2.2 CGO (ceria-gadolinia) barrier layer

Generally, the dense YSZ electrolyte layer and the NiO–YSZ anode support were chosen as the joining parts to the metal interconnect. This is because there is no CGO barrier layer for the traditional SOFC half-cell. However, for advanced planar anode-support SOFC cells, a thin porous CGO barrier layer is fabricated between the YSZ electrolyte and the cathode to increase cell stability. The size of the CGO barrier layer is the same as that of the YSZ electrolyte. Thus, the CGO layer can also be selected as the joining part for integrated SOFC sealing.

Indeed, Ag–CuO (or Ag–Cu) can present good wettability on dense or porous CGO with a contact angle of ~20° when 8% CuO is used [13,61]. Specifically, the porous CGO barrier layer on the YSZ electrolyte was chosen as the joining surface of the half-cells. Accordingly, Ag–Cu filler was first employed to join the CGO to aluminized ferritic SS (Al-Crofer 22 H) [61], and then the Al_2O_3 nanoparticles or low-thermal-expansion Li-SiO_4 particles were added into the Ag–CuO system to increase the joint service reliability (air leakage rate and shear strength) (Table 4) [49,97]. As shown in Fig. 5, $LiAlSiO_4$ particles were homogeneously

Table 4 RAW and RAB of CGOs: wetting and brazing processes, wettability, and joint performance before and after aging

Joining system	Interlayer material	Wetting/brazing condition	Wettability; joint performance	Minimum contact angle; maximum average strength; leak rate; fracture energy	Ref.
CGO	Ag-0-8CuO	1050 °C × 30 min	Contact angle	22°	[13]
CGO CGO/Al–Crofer 22 H	Ag-0-8Cu	1000 °C × 20 min 1000 °C × 20 min × 100 kPa	Contact angle shear strength (SLO)	18° 39±3 MPa 38±2 MPa, 800 °C × 250 h, air-aged 35±3 MPa, 800 °C × 250 h, $4H_2 + 50H_2O + N_2$-aged	[61]
CGO/Al–Crofer 22 H	Ag–8CuO–8%Al_2O_3	1050 °C × 30 min × 160 kPa	Air leak rate	(2.1–2.7)×10^{-3} sccm·cm^{-1}, 800 °C × 300 h, air-aged, $4H_2 + 50H_2O + N_2$-aged	[97]
CGO/Al–Crofer 22 H	Ag–2CuO-2-8 wt% $LiAlSiO_4$	970 °C × 20 min × 160 kPa	Shear strength (SLO) air leak rate	62±6 MPa, (1.2–1.4)×10^{-3} sccm·cm^{-1} 55±5 MPa, 800 °C × 300 h, $4H_2 + 50H_2O + N_2$-aged	[49]
CGO/Ce/Co–AISI 441	Ag-0-2 wt% SiO_2	(930–960) °C × 30 min × 200 kPa	He leak rate, fracture energy (4PB, notched multilayer)	5.4×10^{-4} sccm·cm^{-1}, 96.5 J·m^{-2} 88.9 J·m^{-2}, 800 °C × 500 h, air-aged 81.7 J·m^{-2}, 800 °C × 500 h, $5H_2$–$95N_2$-aged	[98]

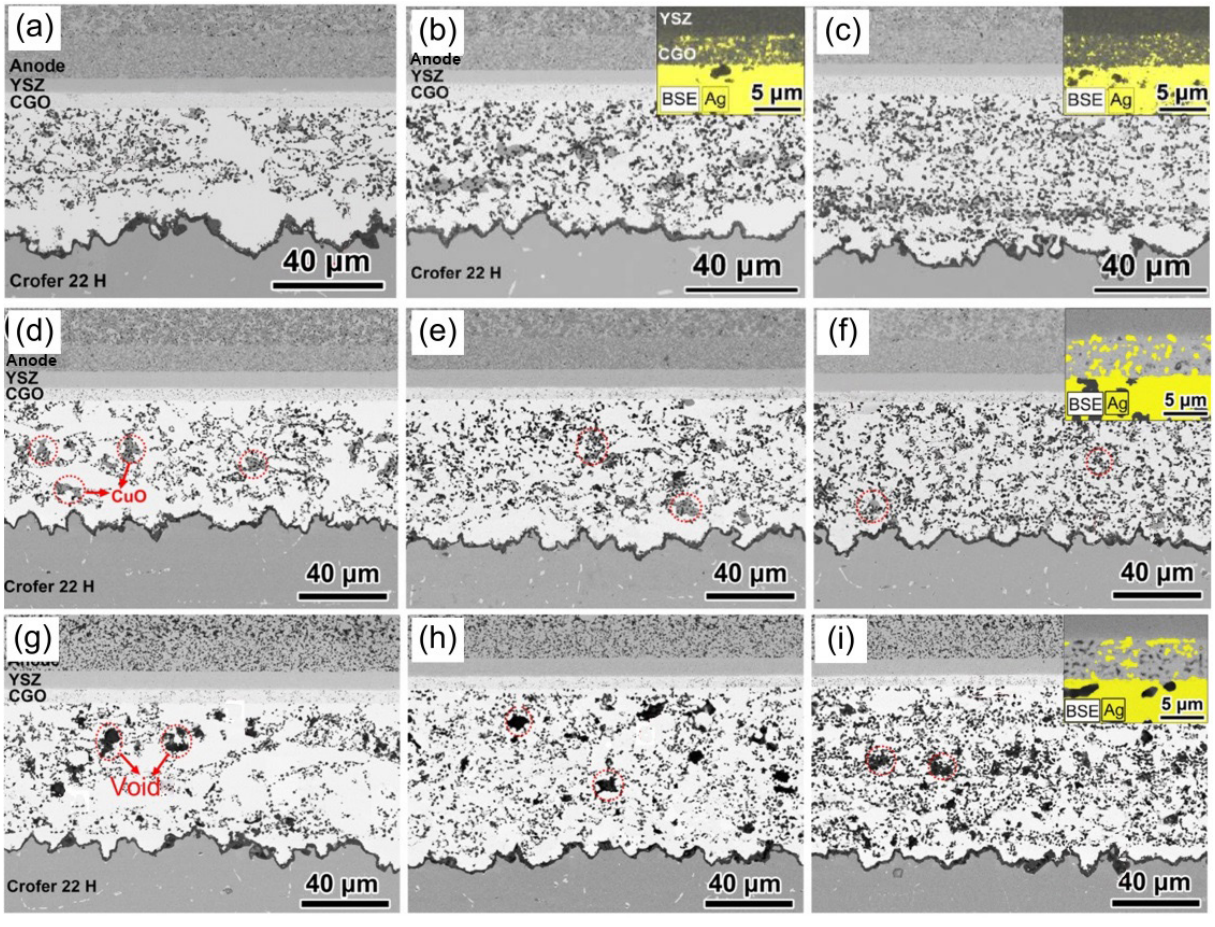

Fig. 5 Cross-sectional SEM images of CGO/Al-Crofer 22 H joints (a–c) before and after aging at 800 °C for 300 h in (d–f) air or (g–i) $4H_2 + 50H_2O + N_2$ atmosphere: (a, d, g) Ag–2CuO–2 wt% $LiAlSiO_4$, (b, e, h) Ag–2CuO–4 wt% $LiAlSiO_4$, and (c, f, i) Ag–2CuO–6 wt% $LiAlSiO_4$. Reproduced with permission from Ref. [49], © Elsevier B.V. 2020.

dispersed in the Ag-based interlayer of the joints, and the Ag-based interlayer was tightly brazed to the CGO layer and the Al-Crofer 22 H before and after aging at 800 °C for 300 h, without any interface delamination. Moreover, after long-term aging in air, the joints remained dense and were devoid of any defects, with detectable CuO precipitates (Figs. 5(g)–5(i)). However, after long-term aging in a $4H_2 + 50H_2O + N_2$ atmosphere, no CuO phase was detected in the Ag-based interlayer due to the reduction of CuO by diffused hydrogen, leaving voids (Figs. 5(g)–5(i)). The addition of $LiAlSiO_4$ particles to Ag–CuO enhances the shear strength of the CGO/Al-Crofer 22 H joint by ~60%, and the shear strength of the Ag–CuO and Ag–CuO–$LiAlSiO_4$ joints decreases by ~10% after aging at 800 °C for 250 or 300 h in a reducing atmosphere due to the production of a small number of voids resulting from the decomposition and/or reduction of $CuAl_2O_4$ and CuO [49,61]. The addition of Al_2O_3 nanoparticles or $LiAlSiO_4$ particles in the Ag–CuO braze allows the CGO/Al–Crofer 22 H joint to maintain low air leakage rates ((1.2–2.7)×10^{-3} sccm·cm^{-1}) after sealing and aging in an oxidizing/reducing atmosphere [49,97]. The relatively low decline in joint strength and low

leakage rate can be attributed to a lack of severe degradation (such as interface delamination and reactions) at the interface despite the formation of voids in the interlayer after aging in a reducing atmosphere (Fig. 5) [49]. Moreover, a novel Ag-SiO_2 was employed to join the half-cell (CGO/YSZ/NiO–YSZ) to Ce-/Co-coated AISI 441, indicating excellent gas tightness with a He leakage rate of 5.4×10^{-4} sccm·cm^{-1}, and the fracture energy of the notched multilayer sample was reduced by less than 15% after isothermal aging at 800 °C for 500 h in air or a reducing atmosphere ($5H_2$–$95N_2$) [98]. Therefore, Ag–CuO–Al_2O_3 and Ag–CuO–$LiAlSiO_4$ are the two promising RAB fillers for the CGO barrier layer in terms of the air leakage rate and shear strength, whereas Ag–SiO_2 is the best in terms of the He leakage rate.

2.3 Perovskite oxides

MIEC oxides, such as single-phase LSCF, BSCF, BSCFZ, BCFN, BCFZ, and BCZYYb, and dual-phase GDC–LSCF, GDC–LSM, and $Ce_{0.8}Gd_{0.2}O_{2-\delta}$–$NdBaCo_2O_{5+\delta}$ (GDC–NBCO), are a class of perovskite-type oxide ceramics that contain ionic and electronic carriers and are often employed in high-temperature gas separation systems (oxygen and hydrogen generators) and SOFCs as electrodes or electrolytes. To date, only Ag, Ag–CuO (or Ag–Cu), and Ag–Cu–TiH_2 systems have been employed to carry out the RAW and RAB of these MIEC oxides (Tables 5 and 6) [3,18–20,40,99–124]. These MIEC oxides are commonly selected to join SS (such as Crofer 22 APU, Crofer 22 H, AISI 314, AISI 310S, AISI 441, and SUS460 FC), high-temperature alloys (including Fecralloy, Kanthal APM, Haynes 214, and Inconel 600), and themselves (Table 6). LSCF was first employed for RAW and RAB since the early 2000s. The LSCF was well wetted by Ag-CuO (or Ag-Cu), with a minimum contact angle of ~20°-30° at 950-1100 °C for 10-30 min, which mainly depended on the CuO content and temperature (Table 5) [3,99–102]. In fact, CuO cannot react with LSFC, resulting in nonreactive wetting. Specifically, the contact angle decreases greatly as the CuO content increases from 0% to ~4%, decreases gradually to the minimum value of ~25° as the CuO content further increases to ~35%, and finally climbs slightly as the CuO content further increases to ~69% [100]. In particular, the addition of 0.5% TiH_2 to the Ag-2-69Cu system can greatly decrease the contact angle of the Ag–Cu/LSCF system, but a deleterious reaction zone may form at the substrate surface, resulting in grain boundary melting [3,101]. Moreover, the maximum average 3-point bending (3PB) strength of the LSCF/Ag-4CuO/LSCF joint reached ~124 MPa [99], and the LSCF/fecralloy joint can retain hermetic strength after aging at (750-950) °C × 2000 h [102].

Under various experimental conditions, the minimum contact angles of molten Ag–CuO (or Ag–Cu) on BSCF, BSCFZ, BCFZ, BCFN, GDC–NBCO, BTO, and PZT were ~30° [102–104], 45° [102], 37° [102], 20° [105–107], 20° [110], 46° [111,112], and 62° [113], respectively (Table 5). The good wettability of molten Ag-CuO originates from a reactive wetting mechanism in addition to the Ag-CuO/PZT system, which can be attributed mainly to interfacial reactions or exchange reactions ($Cu^{2+} \leftrightarrow Co^{2+}$) between CuO (or Cu–O in the braze) and substrates (including BSCF, BCFN, or GDC–NBCO), resulting in the formation of Cu–Co–O (such as $CoCuO_2$ and $Cu_xCo_{1-x}O$), Ba–Cu–O ($Ba_2Cu_3O_{5+x}$), $BaCo_{0.7-x}Cu_xFe_{0.2}Nb_{0.1}O_{3-\delta}$, and Nd–Ce–Cu–O [104,105,107,110]. The final apparent contact angle was also closely related to the formation of a ridge near the triple line caused by the rapid interfacial reaction and its pinning effect, which hinders the spread of liquid across the substrate (Fig. 6) [104,105,107].

Generally, the tensile or 4PB strength values of BSCF/SS joints are lower than 35 MPa before and after aging in air [20,103,114–116], and the He leakage rates ($(2\text{-}4)\times10^{-2}$

Table 5 RAW of perovskite oxide ceramics: wetting process, contact angle, and interfacial products

Substrate	Drop material	Wetting condition	Minimum contact angle (°)	Interfacial product	Ref.
LSCF	Ag-0-4Cu Ag-0-4Cu-0.5TiH_2	(950-1100) °C × 15 min	~39 ~31	—	[3]
LSCF	Ag-0-69.3Cu	(1000-1100) °C × 15 min	~25±5	—	[99]
LSCF	Ag-0-69.3Cu	(950-1100) °C × 15 min	~25	—	[100]
LSCF	Ag-1-69Cu Ag-1-69Cu-0.5TiH_2	(1000-1100) °C × 10 min	~25 ~9	—	[101]
LSCF	Ag-2-50Cu	1020 °C × 30 min	~17	—	[102]
BSCF	Ag-1-16Cu	955 °C × 12 min	34	—	[103]
BSCF	Ag-1-8CuO	1000 °C × 30 min	52±4	Cu-Co-O	[104]
BSCF BSCFZ BCFZ	Ag-2-50Cu Ag-2-20Cu Ag-2-20Cu	1020 °C × 30 min	~27 ~45 ~37	—	[102]
BCFN	Ag-6.6Cu	970 °C × (0-20) min	~20	$CoCuO_2$, $Ba_2Cu_3O_{5+x}$	[105]
BCFN	Ag-0-16Cu	(955-1000) °C × 0 min	~20	—	[106]
BCFN	Ag-0-16Cu	980 °C × 5 s	21	$Cu_xCo_{1-x}O$, $BaCo_{(0.7-x)}Cu_xFe_{0.2}Nb_{0.1}O_{3-\delta}$	[107]
BZCYYb	Ag-0-8 wt% CuO	1010 °C × 20 min	45.1	—	[108]
BZCYYb	Ag-0-8CuO	1000 °C × 30 min	48±3	—	[109]
GDC–NBCO	Ag-0-15.8Cu	1000 °C × 10 min	20	Ba-Cu-O, Co-Cu-O, and Nd-Ce-Cu-O	[110]
BTO	Ag-0-10Cu	980-1100 °C	46±1	—	[111]
BTO BZT	Ag-0-3Cu	1000 °C × 30 min	46 51	CuO	[112]
PZT	Ag-0-10 wt% CuO Ag-1-10 wt% V_2O_5; Ag-0.5-10 wt% PbO; Ag-1-10 wt% [PbO-$14TiO_2$]	1050/1100 °C × 30 min 1000 °C × 30 min 1000 °C × 30 min 1000 °C × 30 min	62 83 ~90±3 ~82	—	[113]

Table 6 RAB of perovskite oxide ceramics: joining process, joint performance, and interfacial products

Joining system	Interlayer material	Brazing condition	Joint performance	Maximum average strength, electrical resistivity; leak rate, oxygen permeation flux	Interfacial product	Ref.
LSCF/preoxidized-fecralloy	Ag–2,4CuO	1100 °C × 30 min	—	—	$CuAlO_2$	[3]
LSCF/LSCF	Ag-0-69.3Cu	1050 °C × 30 min	3PB strength (rectangular)	~124 MPa	—	[99]
LSCF/LSCF	Ag-1-69Cu –0.5TiH_2	1050 °C × 30 min	Electrical resistivity	0.85 Ω·cm, 750 °C × 250 h	$SrTiO_3$	[101]
LSCF/fecralloy	Ag–4Cu	1020 °C × 30 min	N_2 leakage	Hermetic, (750–950) °C × 2000 h	—	[102]
AISI314/BSCF/AISI 314	Ag-1-16Cu	955 °C × 12 min	Tensile strength	14 MPa	—	[103]
AISI314/BSCF/AISI 314	Ag–3Cu (Cu/Ag/Cu foil)	955 °C × 12 min	Tensile strength	14 MPa 6.1 MPa, 850 °C × 500 h, air-aged	—	[114]
BSCF/Crofer 22 H	Ag–3Cu, Ag–3Mo	955 °C × 12 min	4PB strength (round)	23 MPa	—	[20]
BCFZ/fecralloy	Ag–4Cu	1020 °C × 30 min	N_2 leakage	Hermetic, (750–950) °C × 100 h	—	[102]
BSCF/(Crofer22APU, Kanthal APM, Haynes 214, EN 1.4841)	Ag	940 °C × 20 min × ~900 kPa	He leak rate; oxygen permeation flux	$(2–4)\times10^{-2}$ mbar·L·s^{-1}·cm^{-1} ~1.1 mL·cm^{-2}·min^{-1}, 830 °C	$BaCrO_4$	[19]
BSCF/AISI 314 BSCF/preoxidized-AISI 314 BSCF/preoxidized-X8CrAl25-5	Ag–3Cu (Cu/Ag/Cu foil)	970 °C × 6 min × 5 kPa	4PB strength (round, double joint)	16.6 MPa, 850 °C × 1000 h, air-aged 32.9 MPa, 850 °C × 1000 h, air-aged 25.2 MPa, 850 °C × 1000 h, air-aged	—	[115]
BSCF/Al-AISI314 BSCF/NiCoCrAlReY-AISI314 BSCF/YSZ–NiCoCrAlReY-AISI314	Ag–3Cu (Cu/Ag/Cu foil)	970 °C × 6 min	4PB strength (round, double joint)	30.3 MPa, 850 °C × 1000 h, air-aged 35.2 MPa, 850 °C × 1000 h, air-aged 31 MPa, 850 °C × 1000 h, air-aged	--	[116]
BSCF/BSCF	Ag-1-25CuO	970 °C × (0–120) min	—	—	—	[117]
BSCF/AISI 314	Ag–3Cu (Cu/Ag/Cu foil)	955 °C × 12 min	—	—	—	[118]
BCFN/AISI 310S	Ag-1-4Cu	970 °C × 0 min (induction brazing)	Oxygen permeation flux	~1 mL·cm^{-2}·min^{-1}, 850 °C × 60 min -200 °C × 30 min × 15 cycles	—	[106]
BCFN/AISI 310S	Ag, Ag–1Cu	965 °C × 12 min	Oxygen permeation flux	~1.6 mL·cm^{-2}·min^{-1}, 875 °C × 30 min -200 °C × 20 min × 11 cycles	—	[119]
BCFN/Ag–Cu	Ag–6.6Cu	980 °C × 0 min (induction brazing)	—	850 °C × (100–1000) h, air or Ar-aged	$Ba_2Cu_2O_5$ Co–Cu–O	[120]
BZCYYb/Crofer 22 APU	Ag-0-8 wt% CuO	1010 °C × 20 min × 160 kPa	Shear strength (SLO)	21.6 MPa	—	[108]
BZCYYb/AISI 441	Ag-0-8CuO	(970–1090) °C× 30 min × ~20 kPa	—	Intact and dense, 600 °C × 300 h, 4H_2 + 96 Ar-aged or 50air + 50H_2O-aged	$Cu_2Yb_2O_5$, $BaCr_2O_4$	[109]
BZCYYb/AISI 441 BZCYYb/$Mn_{1.5}Co_{1.5}O_4$–AISI 441	Ag–2CuO	970 °C × 30 min × ~20 kPa	Shear strength (SLO)	15.9 MPa 20.9 MPa dense, 600 °C × 300 h, 4H_2 + 96Ar-aged or 50air + 50H_2O-aged	$BaCuO_2$	[121]
GDC–LSCF/GDC–LSCF	Ag–10 wt% CuO	1050 °C × 30 min	Shear strength (SLO)	59.3 MPa 40.2 MPa, 800 °C × 24 h, air-aged	—	[122]
GDC–LSCF/AISI 310S GDC–LSCF/inconel 600 GDC–LSCF/Crofer 22 APU	Ag–10 wt% CuO	1050 °C × 30 min	Shear strength (SLO)	93 MPa; ~31 MPa, 800 °C × 24 h, air-aged 66 MPa; ~48 MPa, 800 °C × 24 h, air-aged 91 MPa; ~88 MPa, 800 °C × 24 h, air-aged	—	[18]
GDC–LSM/Inconel 600 GDC–LSM/Fecralloy GDC–LSM/AISI 310S GDC–LSM/Crofer 22 APU	Ag–10 wt% CuO	1050 °C × 30 min	Shear strength (SLO)	47 MPa; ~41 MPa, 800 °C × 24 h, air-aged 51 MPa; ~43 MPa, 800 °C × 24 h, air-aged 72 MPa; ~45 MPa, 800 °C × 24 h, air-aged 89 MPa; ~73 MPa, 800 °C × 24 h, air-aged	—	[40]
GDC–LSM/SUS460 FC	Ag–10 wt% CuO	1050 °C × 30 min	Shear strength (SLO) 3PB strength	60±8 MPa 78±6 (RT) 45±7 (800 °C) 29±7 (850 °C)	—	[123]
GDC–LSM/Crofer 22 APU	Ag–10 wt% CuO	(1000–1100) °C × (10–60) min	Shear strength (SLO)	100±6 MPa	—	[124]
BTO/BTO	Ag–10Cu	(980–1100) °C	Shear strength (SL)	46±4 MPa	—	[111]
PZT/PZT	Ag-1-10 wt% CuO	1050/1100 °C × (5–60) min	4PB strength (rectangular)	71 MPa	—	[113]

mbar·L·s^{-1}·cm^{-1}) of BSCF/SS joints are far higher than those of YSZ/SS joints (Tables 3 and 6) [19,87,88]. Indeed, high-temperature long-term aging in air can cause joint strength degradation due to an increase in microstructural defects, such as the thickness and porosity of the mixed oxide layers, and interface delamination, whereas surface preoxidization and coating of steel components can obviously reduce joint strength degradation [115,116]. For example, the strength degradation of BSCF/BSCF/Ag–3CuO/AISI 314 after aging at 850 °C × 1000 h in air was reduced from 75% to 59% because of the preoxidization of the steel component at 1050 °C, and the chromium poisoning of BSCF/SS joints was effectively suppressed [115]. Aluminous AISI 314 can inhibit chromium diffusion and the growth of mixed oxide layers, and the NiCoCrAlReY coating can lead to well-wetted interfaces and prevent chromium poisoning of the BSCF ceramics, resulting in low-defect microstructures and increasing the joint strength from ~17 to 35 MPa [116]. In fact, grain coarsening can also be produced around the reaction zone as the CuO content increases, and the pore size increases with increasing brazing time and CuO content, as demonstrated by phase field simulations (Fig. 7) [117].

In particular, sleeve joints between BCFN membrane tubes and steel (310S) supports were designed and achieved by induction brazing in air using a Ag–1Cu filler after the computation of residual stresses (Fig. 8) [106]. However, the hermeticity and average oxygen permeation flux of sleeve joints fabricated by conventional RAB were more stable than those of sleeve joints produced by induction brazing [106,119]. Moreover, the copper oxides in the interfacial reaction layer agglomerated and grew up, diffused along the pores into the BCFN matrix, and continued to participate in the interfacial reactions with prolonged aging time at 850 °C in air, resulting in an increased thickness of the interfacial reaction layer [120]. However, the interfacial product $Ba_2Cu_2O_5$ severely decomposed after long-term aging at 850 °C in Ar, leaving holes in the interfacial reaction layer [120].

Compared with traditional oxygen-ion-conducting SOFCs, BCZYYb is a type of hydrogen-ion-conducting SOFC, i.e., a protonic ceramic fuel cell (PCFC), which has several advantages, such as a lower operating temperature (400–600 °C) and higher power density (> 2 W·cm^{-2}) [108,125]. To date, only Cao's group investigated the RAW and RAB of BCZYYb electrolyte using Ag–CuO as the filler metal, indicating that a contact angle of 45°–50° was obtained at approximately 1000 °C due to the segregation of the CuO-rich liquid phase (L_1) on the substrate surface and the interfacial reaction between L_1 and BCZYYb [108,109]. Moreover, a composite reaction layer ($Cu_2Yb_2O_5$/$BaCr_2O_4$) formed at the Ag/BZCYYb interface (Fig. 9) [109], where Cr originated from AISI 441 because of the absence of a

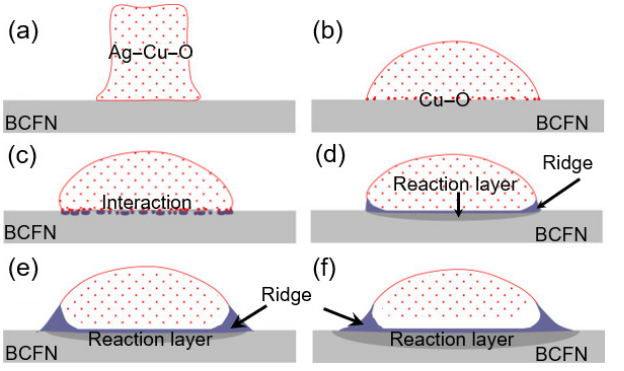

Fig. 6 Schematic representation of reactive spreading model and formation of ridges for Ag–Cu/BCFN system in air. Reproduced with permission from Ref. [115], © Elsevier Ltd and Techna Group S.r.l. 2016.

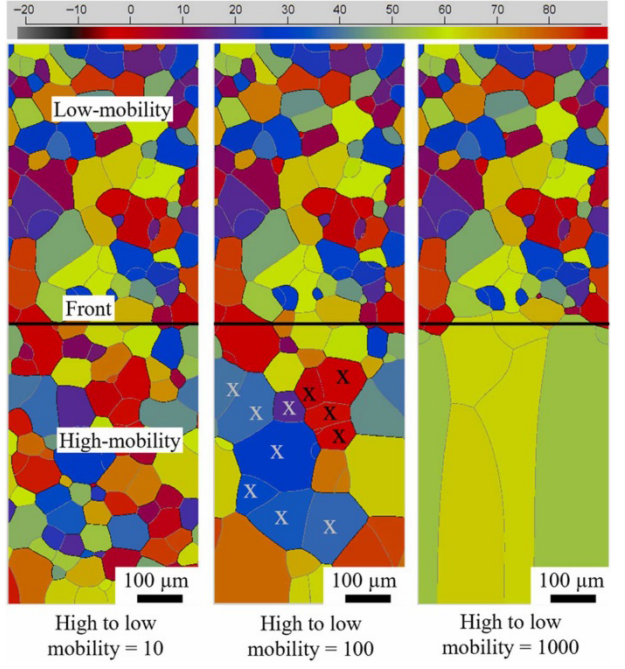

Fig. 7 Snapshot of phase field simulations for different high-to-low mobility ratios in BSCF during RAB using Ag–CuO, demonstrating a progressive elongation of the grains with increasing ratio. Reproduced with permission from Ref. [117], © Elsevier Ltd. 2022.

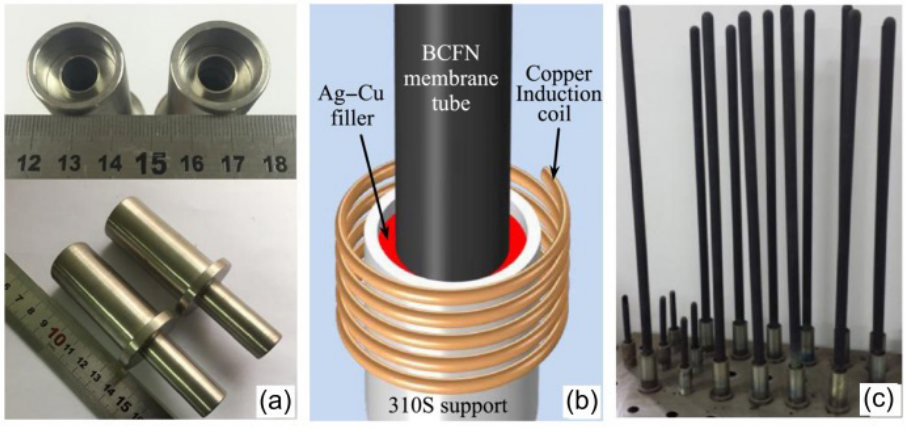

Fig. 8 Induction brazing BCFN membrane tubes to metal supports via a Ag–Cu alloy in air: (a) 310S support, (b) induction brazing, and (c) as-brazed membrane modules. Reproduced with permission from Ref. [106], © Elsevier B.V. 2017.

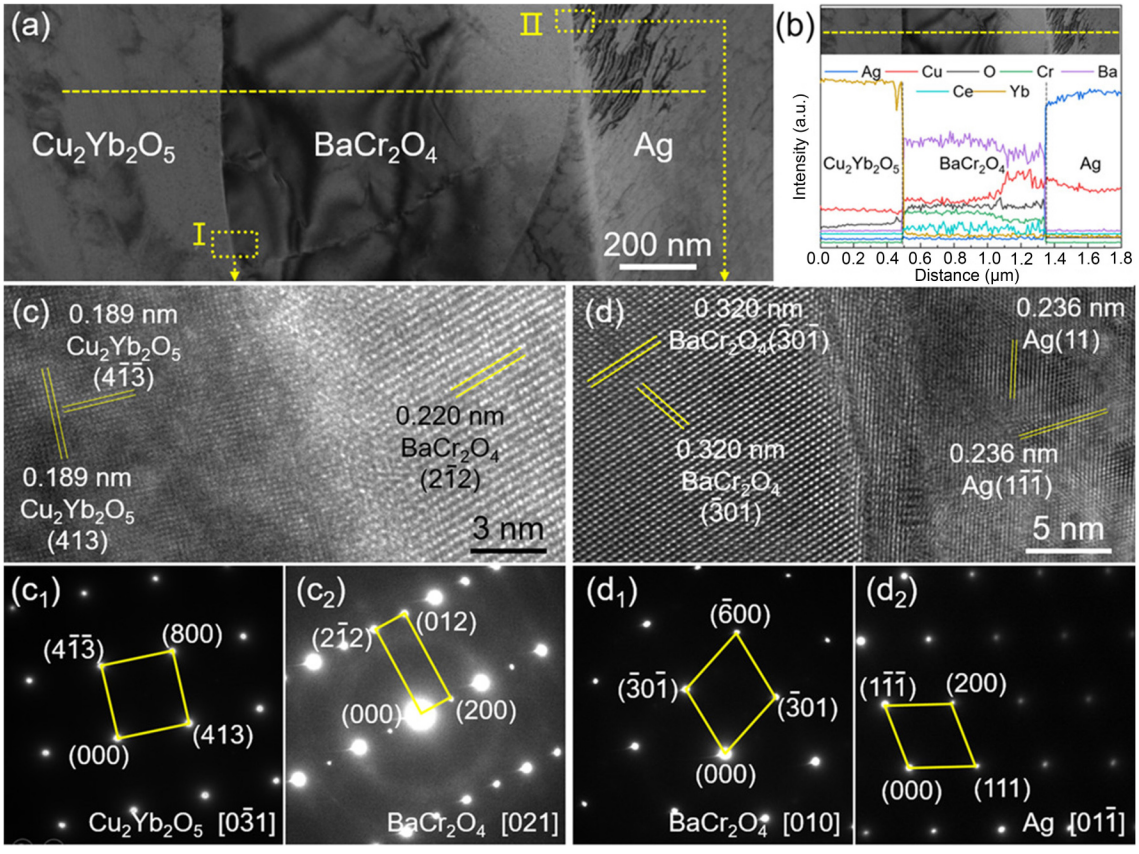

Fig. 9 BZCYYb/Ag–2CuO interface in BZCYYb/Ag–2CuO/AISI 441 joint: (a) TEM image of reaction layer and (b) corresponding elemental distribution, HRTEM images at (c) $Cu_2Yb_2O_5/BaCr_2O_4$ and (d) $BaCr_2O_4$/Ag interfaces and corresponding SAED patterns. Reproduced with permission from Ref. [109], © American Chemical Society 2021.

coating on the steel. Moreover, a visible difference in joint strength existed in BZCYYb/SS joints due to the difference in TEC between SS (Crofer 22 APU and AISI 441) and BCZYYb (Table 6), and an Mn–Co spinel coating on AISI 441 can effectively increase the joint strength by 31% by preventing the reaction of Cr with the electrolyte and reducing the formation of brittle compounds along the BZCYYb interface [121].

Dual-phase oxygen transport membranes (OTMs) are commonly composed of perovskite oxides and oxygen-ion conductors. Among these materials, GDC–LSFC and GDC–LSM are two typical and promising materials because of their high oxygen permeation flux and structural stability. The SLO shear strengths of GDC–LSCF/SS and GDC–LSM/SS joints were more or less different, possibly because of the differences in the TEC and composition of the steels used, which ranged from ~50 to 100 MPa [18,40,122–124]. Moreover, isothermal aging at 800 °C for 24 h can cause joint shear strength degeneration of ~10%–60% [18,40,122].

In addition, the BTO piezoelectric ceramics exhibited good wettability in contact with liquid Ag–Cu alloys in air, and BTO/BTO joints obtained using Ag–10Cu had an average strength comparable to that of monolithic ceramics [111]. On the other hand, in BZT, the wettability decreases with increasing Zr content due to the increased bandgap energy of the ceramics [112]; no study has reported the effect of dopants. The PZT piezoelectric ceramics were hardly wetted and brazed in air by Ag–V_2O_5, Ag–PbO, or Ag–PbO–TiO_2 at 1000 °C for 30 min, with contact angles of over 80° and joint 4PB strengths of less than 10% of the monolithic PZT fracture strength [113]. However, the PZT ceramics can be wetted and brazed by Ag–CuO, resulting in a minimum contact angle of 62°, the highest joint 4PB strength of 71 MPa, and an average joint 4PB strength of 64 MPa (~62% monolithic PZT fracture strength) [113].

In short, Ag–CuO (or Ag–Cu) can wet the abovementioned perovskite oxides well except for PZT, and obvious degradation in strength can occur in the joints between MIEC oxides and SS, although hermetic joints can be produced by using a Ag–CuO filler before and after isothermal aging in an oxidizing or reducing atmosphere. In particular, surface preoxidation and coating on metal components are two effective measures for enhancing joint mechanical properties and aging resistance.

3 Structural ceramic components

Al_2O_3 ceramics and three typical nonoxide ceramics (SiC, AlN, and Si_3N_4) are often used as structural components in aerospace, military, machinery, metallurgy, electronics, nuclear, and other fields due to their outstanding high-temperature stability and wear and corrosion resistance [126–128]. For example, some of them can be applied in advanced power generation equipment, such as gas turbines, combustion engines, heat exchangers, and burners [1,129].

3.1 Al_2O_3

As described above, the Ag–CuO (or Ag–Cu) brazing fillers were most commonly used in RAW and RAB of ceramics. In addition to the Ag–CuO (or Ag–Cu) fillers [1,4,11,68,130–136], Al [137], Ag–Al [138–140], Ag–SiO_2 [141], and Ag–Nb_2O_5 [142] have also been employed for the RAW and RAB of Al_2O_3 ceramics, especially Ni [140], Ti (Table 4) [68,140], Pt [143], and TiH_2 [144], which have been added to the Ag–CuO or Ag–Cu system (Table 7). The contact angle of the Ag–CuO/Al_2O_3 system gradually

decreased from ~76° to 3° as the CuO content increased from 1% to 69% when the sessile drop experiments were performed at 1000 or 1100 °C for 15 min. The contact angle of the Ag–80CuO/Al_2O_3 system was ~6°, even though the Ag–80CuO braze was not expected to fully melt until ~1027 °C (Fig. 10(a)) [1]. Similarly, the contact angle of the Ag–Nb_2O_5/Al_2O_3 system gradually decreased from ~71.6° to 32.5° as the Nb_2O_5 content increased from 0.5% to 12% when wetting experiments were performed at 1150 °C for 30 min [142]. Moreover, small additions of Ti to Ag–Cu brazes decreased the contact angle of the Ag–Cu/Al_2O_3 system, and the optimal Ti content depended on the Cu content and wetting temperature. Specifically, the contact angle was reduced from ~31° to 6° at 1150 °C when 4% Ti was added to Ag–68Cu, which mainly originated from the infiltration of the ceramic substrate along the grain boundaries caused by the addition of Ti [68].

Indeed, most RAB of Al_2O_3 ceramics, SS, aluminized Q235 steel, Ni alloys, and Ti6Al4V were performed via Ag–CuO- or Ag–Cu-based fillers. The CuO content ranged from 0 to 80%, and the brazing temperature and holding time ranged from 970 to 1100 °C and from 5 to 60 min, respectively (Table 7). Owing to the differences in the brazing process (brazing conditions, brazing filler thickness and form, i.e., paste, foil, and sheet) and measurement methods of joint strength, the room-temperature Al_2O_3/Al_2O_3 joint strength (including 4PB, shear, and tensile modes) of unaged samples varies greatly from < 50 MPa to > 200 MPa. In particular, the average 4PB strength of the Al_2O_3/Al_2O_3 joint increased to a maximum of 221 MPa as the CuO content increased from 1% to 8% and then sharply decreased to 73 MPa when the Ag–80CuO filler was employed (Fig. 10(a)) [1]. After aging at 800 °C for 100 h in static air, the

Table 7 RAW and RAB of Al_2O_3 ceramics: wetting and brazing processes, contact angle, joint performance, and interfacial products

Wetting substrate/ joining system	Drop materia/ brazing filler	Wetting/brazing condition	Wettability/joint performance	Minimum contact angle/ maximum average strength	Interfacial product	Ref.
Al_2O_3 Al_2O_3/Al_2O_3	Ag-1-80Cu	(1000-1100) °C × 15 min; (1000-1100) °C × 30 min	Contact angle 4PB strength (rectangular)	~3° 221 MPa	$CuAlO_2$	[1]
Al_2O_3/Al_2O_3	Ag-0-8CuO	1000 °C × 60 min × ~5 kPa	4PB strength (rectangular)	188 MPa ~180 MPa,1000 °C × 100 h, air-aged < 40 MPa, 1000 °C × 100 h, H_2-aged	—	[4]
Al_2O_3/Al_2O_3	Ag-2/8CuO	(980-1100) °C × 30 min	Hermeticity	No degradation, 800 °C × 100 h air/H_2-aged Pore formation, 800 °C × 1000 h, air/H_2-aged	$CuAlO_2$	[130]
Al_2O_3/Al_2O_3	Ag-0-8Cu	1000 °C × 60 min	4PB strength (rectangular)	~148 MPa ~36.1 MPa, 800 °C × 100 h, H_2-aged ~114 MPa, 800 °C × 100 h, air-aged	$CuAl_2O_4$	[131]
Al_2O_3 Al_2O_3/Al_2O_3	Ag-4-90Cu Ag-4-68Cu-0.5-8Ti Ag-8Cu Ag-8Cu-8Ti	(970-1150) °C × 20 min (970-1150) °C × 20 min (970-1150) °C × 20 min 1150 °C × 20 min	Contact angle — —	~22° 6° — —	(Cu,Al)O (Cu,Al,Ti)O	[68]
Al_2O_3	Ag, Ag-4 wt% CuO	1000 °C × 5 min	Contact angle	71.1°	$CuAl_2O_4$	[132]
Al_2O_3/Al_2O_3	Ag-7-16CuO	(1050-1100) °C × (0-30) min	4PB strength (rectangular)	190±60 MPa	—	[133]
ZTA/ZTA ZTA/Ni alloy/ZTA	Ag–2 wt%CuO	1100 °C × 30 min	4PB strength (rectangular)	190 MPa; 62 MPa	—	[134]
Al_2O_3/Crofer 22 APU	Ag–4 wt%Cu	(1000-1100) °C × (5-30) min	Shear strength (SL)	115±10 MPa	—	[11]
Al_2O_3/Q235 Al_2O_3/Al-Q235	Ag–12CuO	1050 °C × 15 min	—	—	$CuAl_2O_4$	[135]
ZTA/Al-Ti6Al4V	Ag–2CuO	(970–1090) °C × 15 min	Shear strength (SLO)	~56.8 MPa; ~52.3 MPa, 800 °C × 5 h × 24 cycles, air-aged	$CuAl_2O_4$	[136]
Al_2O_3/Al_2O_3	Al	850 °C × 240/480 min	4PB strength (rectangular)	94 MPa 114 MPa, 850 °C × 96 h, air-aged	—	[137]
Al_2O_3/Al_2O_3	Ag-0-35.1Al	(600-1100) °C × 6 min	4PB strength (rectangular)	79 MPa (Ag)	—	[138]
Al_2O_3/Al_2O_3	Ag-0-10Al Ag-5Al-0-8Cu	1000 °C × 60 min	4PB strength (rectangular)	~78 MPa (Ag) ~118 MPa	—	[139]
A_2O_3/X1CrTiLa22	Ag–4Cu Ag–8Cu Ag–8Cu–0.5Ti Ag–4Cu–4Ni Ag–0.5Al	1050 °C × 20 min 1050 °C × 20 min 1150 °C × 20 min 1350 °C × 20 min 1150 °C × 20 min	Contact angle Tensile strength Gas tightness	48°, 64 MPa, gas tight 39°, 65 MPa, gas tight 68 MPa, gas tight 66 MPa, not gas tight 42 MPa, not gas tight	—	[140]
Al_2O_3/Al_2O_3	Ag-0-1.5 wt% SiO_2	1050 °C × 30 min × 200 kPa	Shear strength (SLO)	32 MPa	—	[141]
Al_2O_3 Al_2O_3/Al_2O_3	Ag-0-12Nb_2O_5	1050 °C × 30 min 1050 °C × 30 min × ~50 kPa	Contact angle Shear strength	~32.5° ~65 MPa	$AgNbO_5$	[142]
Al_2O_3/Al_2O_3	Ag-8CuO-0-13.6 wt% Pt	1050 °C × 30 min × 1 kPa	Shear strength (SLO)	~46 Mpa ~34 MPa (600 °C)	$CuAl_2O_4$	[143]
A_2O_3 A_2O_3/X2CrNiMo 17-2-2 A_2O_3/X1CrTiLa22 A_2O_3/X10CrAlSi18	Ag-0–8CuO–0.5TiH_2 Ag–4CuO–0.5TiH_2	1000 °C × 10 min 1000 °C	Contact angle —	~33° —	—	[144]

strength of the Al_2O_3/Ag-0-8CuO/Al_2O_3 joint 4PB decreased slightly, and the joint strength sharply decreased to ~40 MPa after aging at 800 °C for 100 h in flowing H_2 (Fig. 10(b)) [4]. That is, the Ag–CuO-based fillers cannot endure a reducing atmosphere at higher temperatures for a long time since CuO can be reduced into elemental Cu, resulting in the generation of pores at the interface and a sharp decrease in joint strength [4,130]. To resolve this problem, Ag–SiO_2 [141] and Ag–Nb_2O_5 [142] fillers were recently developed. However, the Al_2O_3/Al_2O_3 joint shear strength values were relatively low because there were no interfacial reactions between these two fillers and the Al_2O_3 substrate. In particular, Nb_2O_5 can react with Ag to form $AgNbO_5$ at the interface, but excessive addition of Nb_2O_5 can cause the formation of a large amount of $AgNbO_5$ and the remaining Nb_2O_5 in the

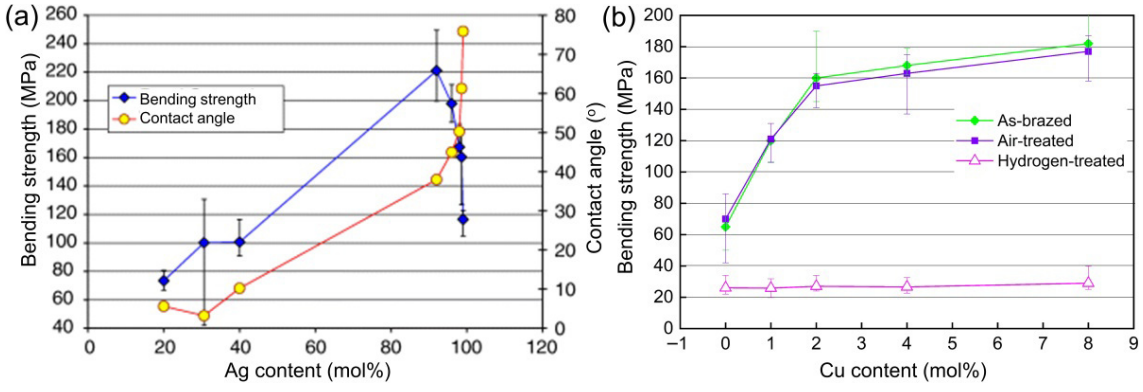

Fig. 10 (a) Room-temperature 4PB strength of Al_2O_3/Ag–Cu/Al_2O_3 RAB joint and contact angle of Ag–Cu/Al_2O_3 RAW system as a function of Ag content. Reproduced with permission from Ref. [1], © The American Ceramic Society 2005; (b) Room-temperature 4PB strength of Al_2O_3/Ag–CuO/Al_2O_3 RAB joint before and after aging at 800 °C for 100 h in static air and flowing H_2 as a function of CuO content. Reproduced with permission from Ref. [4], © The Materials Research Society 2006.

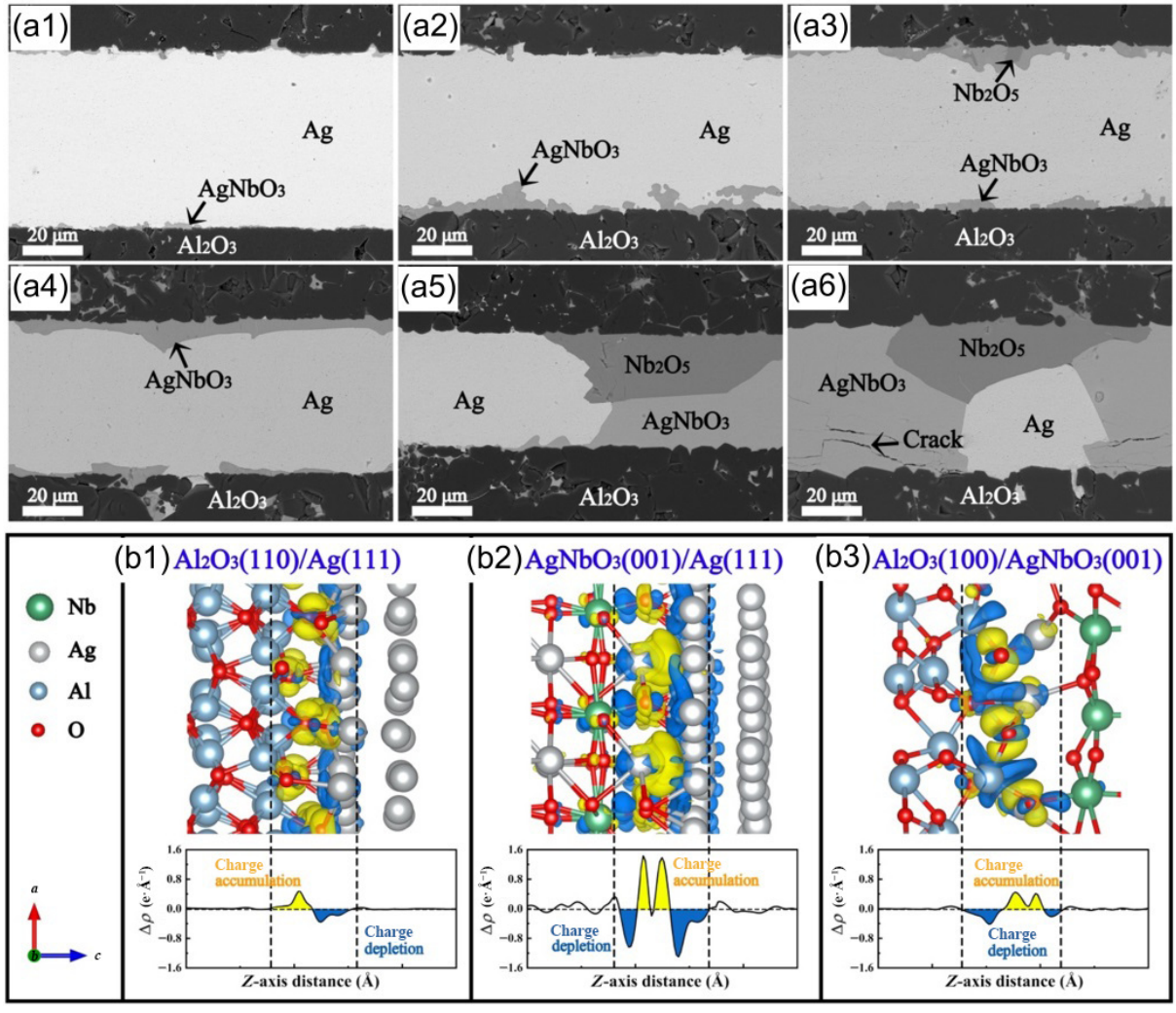

Fig. 11 (a1–a6) Cross-sectional microstructure evolution of Al_2O_3/Ag–Nb_2O_5/Al_2O_3 joints with increasing Nb_2O_5 content from 0.5%, 1%, 2%, 4%, 8%, to 12%. CDDs and corresponding plane-average charge density for (b1) Ag(111)/O–Al_2O_3(110)-top, (b2) Ag(111)/Ag–O–$AgNbO_3$(001), and (b3) Ag–O–$AgNbO_3$(001)/Al_2O_3(100) interfaces. Reproduced with permission from Ref. [142], © The Author(s) 2004.

interlayer, resulting in a discontinuous Ag interlayer and the generation of microcracks in the interlayer (Fig. 11(a)) [142]. In fact, the formation of a small amount of $AgNbO_5$ at the interface can contribute to interfacial bonding due to the formation of Ag–Ag, Al–O, and Ag–O bonds in the $Ag/AgNbO_3/Al_2O_3$ structure (Fig. 11(b)) [142].

Similar to RAW and RAB of YSZ, Ag–CuO can wet and braze the Al_2O_3 ceramics well, and the resulting joints can endure high-temperature aging in air but cannot endure the H_2-containing atmosphere at higher temperatures for a long time. The Ag–Nb_2O_5 may be a promising RAB filler for Al_2O_3, taking into account the joint reliability.

3.2 Nonoxide ceramics

The joining of nonoxide ceramics is commonly performed by AMB, transient liquid-phase bonding (TLPB), and diffusion bonding under high vacuum or a protective atmosphere [95,145–148]. Recently, wetting and brazing of nonoxide ceramics (involving SiC, Si_3N_4, and AlN) were performed at 970–1050 °C for 5–40 min in air [2,149–152]. As shown in Table 8, Wang *et al.* [149] first investigated the RAW and RAB of SiC ceramics by using Ag-1–20V_2O_5, obtained favorable wettability due to the intense interfacial reaction of V_2O_5 and SiC, with the formation of VO_2 and SiO_2 (Fig. 12), and achieved a maximum joint shear strength of ~58 MPa due to the moderate interfacial reaction. Very recently, our group investigated the RAW and RAB of Si_3N_4 and AlN ceramics by using Ag-0–20CuO at 1050 °C for 30 min and obtained a maximum joint shear strength of over 50 MPa [2,152]. In particular, we demonstrated the formation of multiple interfaces, including Ag/SiO_2, Ag/CuO, and Ag/Al_2O_3 (Fig. 13), and concluded that the addition of CuO into Ag can effectively enhance the interfacial bonding and structural stability of Ag/Si_3N_4 and Ag/AlN interfaces through the formation of strong Ag–O ionic bonds, which can be supported by charge density difference (CDD) and density of state (DOS) calculations of related interfaces (Fig. 14) [2,152]. Specifically, the interfacial charge transfer from Ag to Cu-terminated CuO (Cu–CuO), Si-terminated SiO_2 (Si–SiO_2), and Si_3N_4(0001) was quite feeble,

Table 8 RAW and RAB of nonoxide ceramics: wetting and joining processes, wettability, joint strength, and interfacial products

Joining system	Drop/brazing filler	Wetting/brazing condition	Wettability/joint strength	Minimum contact angle/ maximum average strength	Interfacial product	Ref.
SiC SiC/SiC	Ag-1–20V_2O_5	1050 °C × 30 min 1050 °C × 30 min × ~20 kPa	Contact angle Shear strength (SLO)	8°±2° ~58 MPa	VO_2 and SiO_2	[149]
Si_3N_4	Ag-1–16Cu	970 °C × 40 min	Contact angle	17°±1°	SiO_2	[150]
Si_3N_4 Si_3N_4/Si_3N_4	Ag-0–20CuO	1050 °C × 30 min × ~20 kPa	Contact angle Shear strength (pure)	42.5° ~52 MPa	SiO_2	[2]
AlN AlN/AlN	Ag-0–8CuO	1000 °C × 5 min	Contact angle Shear strength (pure)	13.9° 22.6 MPa	$CuAl_2O_4$	[151]
AlN AlN/AlN	Ag-0–20CuO	1050 °C × 30 min 1050 °C × 30 min × ~20 kPa	Contact angle Shear strength (pure)	~6° ~57 MPa	Al_2O_3	[152]

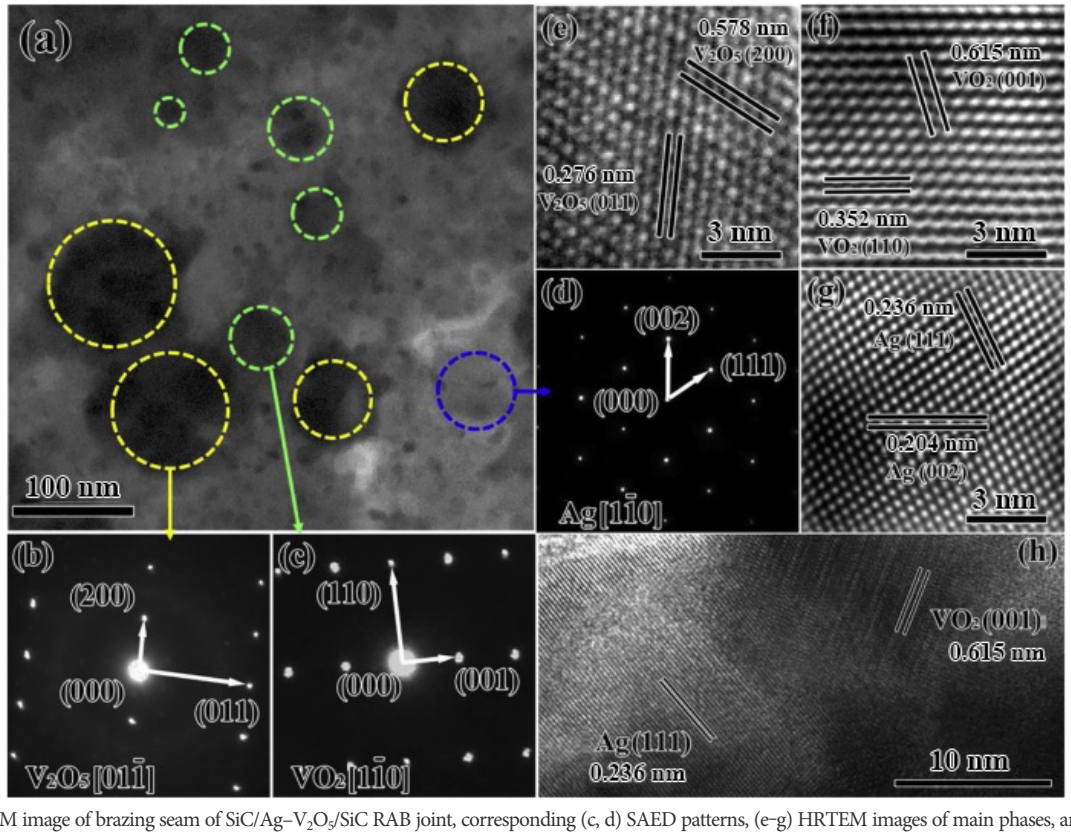

Fig. 12 (a) TEM image of brazing seam of SiC/Ag–V_2O_5/SiC RAB joint, corresponding (c, d) SAED patterns, (e–g) HRTEM images of main phases, and (h) HRTEM image of Ag/VO_2 interface. Reproduced with permission from Ref. [149], © Elsevier Ltd. 2019.

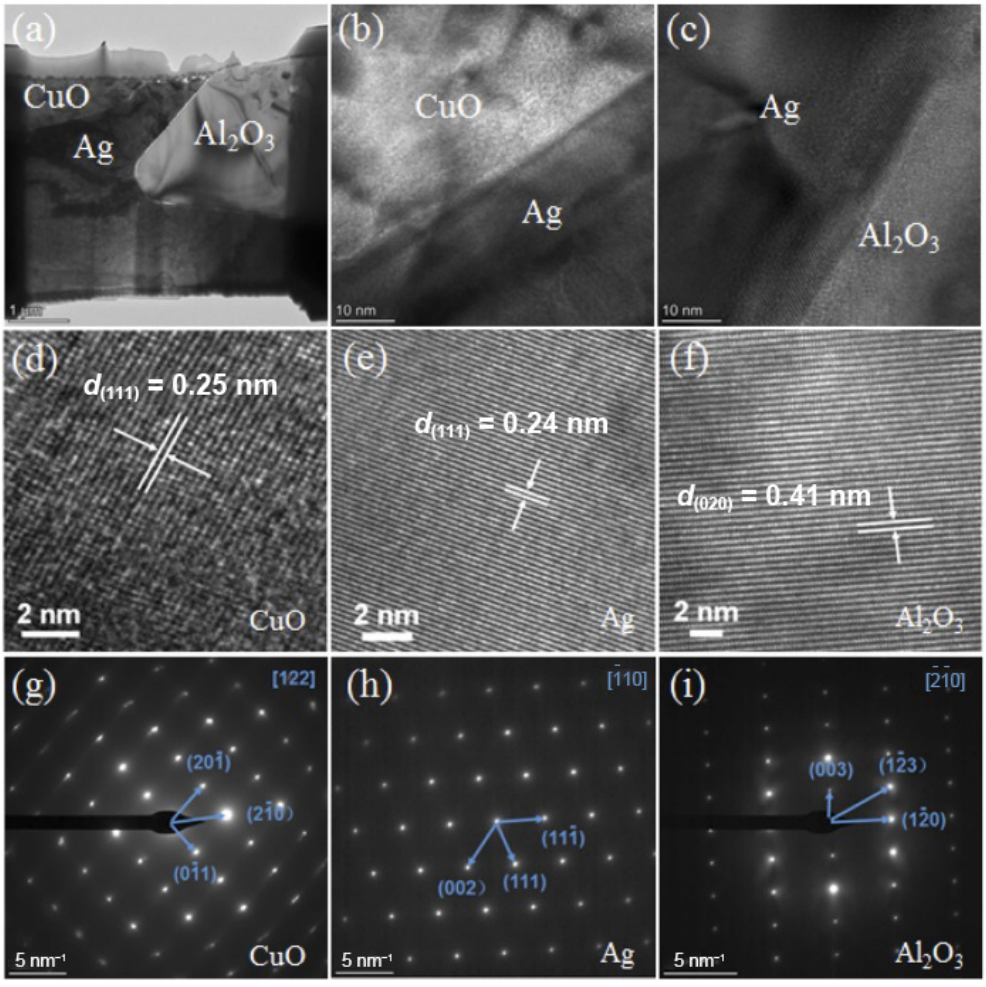

Fig. 13 (a-c) TEM images, (d-f) HRTEM images, and (g-i) corresponding SAED patterns of Ag–12CuO/AlN interface sample. Reproduced with permission from Ref. [152], © Elsevier Ltd. 2024.

whereas significant charge depletion and accumulation around Ag and O atoms were produced at the Ag/O–CuO and Ag/O–SiO_2 interfaces, demonstrating the formation of strong Ag–O ionic bonds (Fig. 14(a)). Moreover, the hybridization between the Ag-4d and O-2p orbitals can cause the formation of new distinct peaks in the DOS of the Ag-4d orbitals in the Ag/O–CuO and Ag/O–SiO_2 interfaces compared with the Ag/Si_3N_4(0001) interface, which can also demonstrate interfacial charge transfer and the formation of Ag–O ionic bonding (Fig. 14(b)). However, these two wetting systems (Ag–CuO/Si_3N_4 and Ag–CuO/AlN) differ substantially in terms of their wetting behavior and minimum contact angle. The contact angle of the Ag–CuO/Si_3N_4 system first decreased quickly and then increased slightly as the CuO content increased from 0 to 20%, with a minimum value of 42.5°, whereas that of the Ag–CuO/AlN system first decreased sharply but then decreased gradually to ~6°. In addition, Wang *et al.* [150] investigated the wettability of Ag–Cu alloys on AlN in air and the interfacial reaction mechanism by employing mass spectrometry and thermodynamic calculations, indicating the formation of solid (Cu–O, SiO_2) and gaseous (N_2, NO, and NO_2) interfacial products. These gaseous products can result in the production of pores at the interlayer/ceramic interface and even in the interlayer with increasing reactive MO_x content, resulting in a decrease in joint strength and gas-tightness. Therefore, adjusting and optimizing the MO_x addition in the RAB fillers is critical for the formation of holes and improving joint reliability.

4 Summary

For RAB of oxide ceramics (YSZ, perovskite oxides, and Al_2O_3), several conclusions can be drawn as follows: (1) Ag–CuO-based fillers cannot endure a reducing atmosphere at high temperatures for a long time since the remaining CuO can be reduced to elemental Cu, resulting in the generation of pores at the interface and a sharp decrease in joint strength and gas-tightness. (2) CuO can also easily react with steels in air at high temperatures, forming dense and thick Cu/Cr/Mn/Fe-oxide reaction layers at the braze/interconnect interface, thus decreasing joint reliability. (3) The operational requirements for the mechanical properties, oxidation resistance, and gas tightness of the RAB joints can be essentially guaranteed by appropriately adjusting the brazing filler system, optimizing the brazing process, optimally choosing high-temperature SS or alloys, and applying suitable coatings.

To date, very limited work has been done on the RAB of nonoxide ceramics, possibly because no current applications exist. The RAB of SiC ceramics has potential application prospects in the semiconductor manufacturing field, such as for vacuum or electrostatic chucks and heat dissipation substrates. Indeed, problems such as very few brazing fillers and lower joint strength remain, and the influence of rules and mechanisms on the service performance of joints are still not clear. Therefore, some urgent work needs to be done for RAB of nonoxide ceramics (especially SiC ceramics), such as the design and development of RAB fillers, investigations on joint service reliability in high-temperature

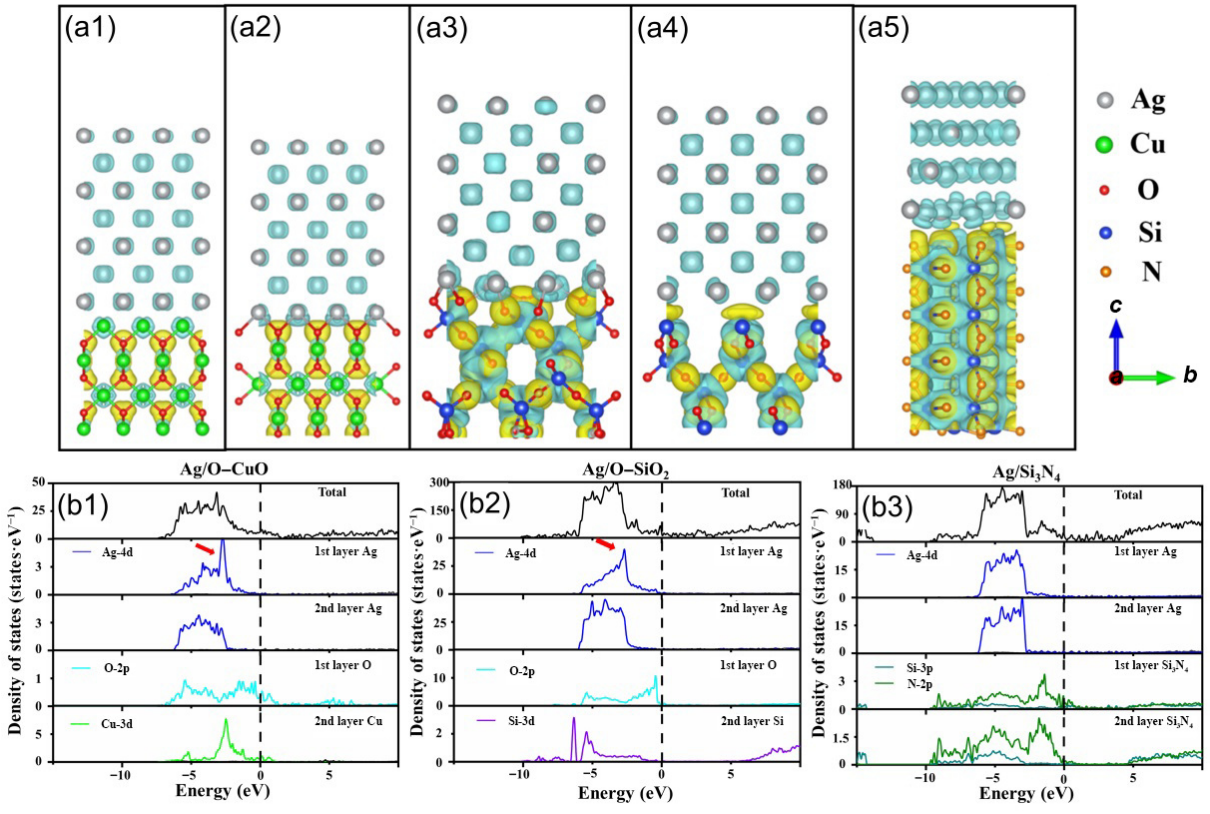

Fig. 14 CDD with an isosurface of 0.006 e/Å for (a1) Ag(110)/Cu–CuO, (a2) Ag(110)/O–CuO, (a3) Ag(110)/O–SiO_2, (a4) Ag(110)/Si–SiO_2, and (a5) Ag(111)/Si_3N_4(0001) interfaces. Local density of states (LDOS) of (b1) Ag(110)/O–CuO, (b2) Ag(110)/O–SiO_2, and (b3) Ag(111)/Si_3N_4(0001) interfaces. Regions in yellow and light blue indicate the buildup and depletion of electrons in (a), respectively. Reproduced with permission from Ref. [2], © Elsevier Ltd. 2021.

O_2-rich or H_2-containing environments, acid or alkali corrosive environments, and potential applications of RAB joints. In addition, the RAB of some new emerging high-entropy ceramics with excellent physicochemical and mechanical properties should also be carried out as soon as possible. For example, high-entropy oxide ceramics are being applied in energy conversion and storage (such as light-heat–electricity conversion devices, SOFCs, and lithium-ion batteries) and in catalytic, electronic, and electrical fields, which may involve the RAB of these materials with other materials.

Moreover, many aspects need to be considered in terms of the RAB process of engineering ceramics, interfacial behavior, and joint service reliability. First, the physicochemical properties of the employed ceramics, metals, and RAB fillers (involving noble metals and oxides), such as TEC, melting point, environmental friendliness, oxidation, reduction, and corrosion resistances, need to be assessed in advance. Second, the service environment (temperature, atmosphere, and the concentration of the acid or base in a solution) needs to be clear. Third, related chemical reactions and resulting defects at the interface need to be predicted and further verified experimentally. Fourth, the oxides in the RAB filler can be screened and optimized via first-principles calculations, machine learning, and high-throughput experiments after the determination of noble metals. Finally, the joint service reliability needs to be investigated in detail by combining experiments and simulations.

Acknowledgements

This work is supported by the National Natural Science Foundation of China (No. 52002153), the Postdoctoral Science Foundation of China (No. 2021M701470), and the Innovation/Entrepreneurship Program (No. JSSCTD202146) of Jiangsu Province.

Declaration of competing interest

The authors have no competing interests to declare that are relevant to the content of this article. The author Guiwu Liu is the Editorial Committee member of this journal.

References

[1] Kim JY, Hardy JS, Weil KS. Effects of CuO content on the wetting behavior and mechanical properties of a Ag–CuO braze for ceramic joining. *J Am Ceram Soc* 2005, **88**: 2521–2527.

[2] Gui XY, Zhang MF, Xu PH, *et al.* Experimental and theoretical study on air reaction wetting and brazing of Si_3N_4 ceramic by Ag–CuO filler metal: Performance and interfacial behavior. *J Eur Ceram Soc* 2022, **42**: 432–441.

[3] Weil KS, Hardy JS. Development of a new ceramic-to-metal brazing technique for oxygen separation/generation applications. In: Proceedings of the 2002 Fossil Energy Conference, 2002.

[4] Kim JY, Hardy JS, Weil KS. High-temperature tolerance of the silver-copper oxide braze in reducing and oxidizing atmospheres. *J Mater Res* 2006, **21**: 1434–1442.

[5] Singh M, Shpargel TP, Asthana R. Brazing of yttria-stabilized zirconia (YSZ) to stainless steel using Cu, Ag, and Ti-based brazes. *J Mater Sci* 2008, **43**: 23–32.

[6] Tillmann W, Anar NB, Wojarski L, *et al.* Microstructure and mechanical properties of reactive-air-brazed 3YSZ/Crofer22APU joints at ambient temperature. *Metallogr Microstruct Anal* 2020, **9**: 529–540.

[7] Yasuda I, Hishinuma M. Lattice expansion of acceptor-doped lanthanum chromites under high-temperature reducing

atmospheres. *Electrochemistry* 2000, **68**: 526–530.
[8] Mori M, Yamamoto T, Itoh H, *et al.* Thermal expansion of nickel-zirconia anodes in solid oxide fuel cells during fabrication and operation. *J Electrochem Soc* 1998, **145**: 1374–1381.
[9] Kiebach R, Engelbrecht K, Grahl-Madsen L, *et al.* An Ag based brazing system with a tunable thermal expansion for the use as sealant for solid oxide cells. *J Power Sources* 2016, **315**: 339–350.
[10] Guo CH, Zhu WW, Shen YX, *et al.* Joining ZTA ceramic by using Dy_2O_3–Al_2O_3–SiO_2 glass ceramic filler. *J Eur Ceram Soc* 2020, **40**: 5819–5828.
[11] Tillmann W, Anar NB, Wojarski L. Mechanical behavior of reactive air brazed (RAB) Crofer 22 APU–Al_2O_3 joints at ambient temperature. *SN Appl Sci* 2020, **2**: 809.
[12] Lin PP, Lin TS, He P, *et al.* Microstructure evolution and mechanical properties of a vacuum-brazed Al_2O_3/Ti joint with Mo-coating on Al_2O_3 and Ti surfaces. *Ceram Int* 2019, **45**: 11195–11203.
[13] Seeharaj P, Atkinson A. Diffusion and conductivity of mixed-conducting Ag/CGO composites. *Solid State Ionics* 2011, **204**: 46–52.
[14] Corbel G, Mestiri S, Lacorre P. Physicochemical compatibility of CGO fluorite, LSM and LSCF perovskite electrode materials with $La_2Mo_2O_9$ fast oxide-ion conductor. *Solid State Sci* 2005, **7**: 1216–1224.
[15] Joo JH, Yun KS, Lee Y, *et al.* Dramatically enhanced oxygen fluxes in fluorite-rich dual-phase membrane by surface modification. *Chem Mater* 2014, **26**: 4387–4394.
[16] Joo JH, Yun KS, Kim JH, *et al.* Substantial oxygen flux in dual-phase membrane of ceria and pure electronic conductor by tailoring the surface. *ACS Appl Mater Inter* 2015, **7**: 14699–14707.
[17] Xu Q, Huang DP, Zhang F, *et al.* Structure, electrical conducting and thermal expansion properties of $La_{0.6}Sr_{0.4}Co_{0.8}Fe_{0.2}O_{3-\delta}$–$Ce_{0.8}Sm_{0.2}O_{2-\delta}$ composite cathodes. *J Alloy Compd* 2008, **454**: 460–465.
[18] Raju K, Muksin, Kim S, *et al.* Joining of metal-ceramic using reactive air brazing for oxygen transport membrane applications. *Mater Design* 2016, **109**: 233–241.
[19] Kiebach R, Engelbrecht K, Kwok K, *et al.* Joining of ceramic $Ba_{0.5}Sr_{0.5}Co_{0.8}Fe_{0.2}O_3$ membranes for oxygen production to high temperature alloys. *J Membrane Sci* 2016, **506**: 11–21.
[20] Bobzin K, Öte M, Wiesner S, *et al.* Characterization of reactive air brazed ceramic/metal joints with unadapted thermal expansion behavior. *Adv Eng Mater* 2014, **16**: 1490–1497.
[21] Lin Y, Zhou W, Sunarso J, *et al.* Characterization and evaluation of $BaCo_{0.7}Fe_{0.2}Nb_{0.1}O_{3-\delta}$ as a cathode for proton-conducting solid oxide fuel cells. *Int J Hydrogen Energ* 2012, **37**: 484–497.
[22] Zhang LM, Shan J, Wang Q. $BaCo_{0.4}Fe_{0.4}Zr_{0.2}O_{3-\delta}$: Evaluation as a cathode for ceria-based electrolyte IT-SOFCs. *J Alloy Compd* 2019, **771**: 221–227.
[23] Qiu P, Liu B, Wu L, *et al.* K-doped $BaCo_{0.4}Fe_{0.4}Zr_{0.2}O_{3-\delta}$ as a promising cathode material for protonic ceramic fuel cells. *J Adv Ceram* 2022, **11**: 1988–2000.
[24] Jia LC, Pei YC, Chen JY, *et al.* High performance $La_{0.5}(Ba_{0.2}Sr_{0.2}Ca_{0.1})Co_{0.8}Fe_{0.2}O_{3-\delta}$–$BaZr_{0.1}Ce_{0.7}Y_{0.1}Yb_{0.1}O_{3-\delta}$ composite cathode for proton-conducting solid oxide fuel cells. *ECS Transactions* 2019, **91**: 1309–1316.
[25] Wang XY, Si XQ, Li MS, *et al.* $Y_2W_3O_{12}$@SiO_2 composite particles for regulating thermal expansion and interfacial reactions in $BaZr_{0.1}Ce_{0.7}Y_{0.1}Yb_{0.1}O_{3-\delta}$/AISI 441 joints. *Compos Part B Eng* 2022, **242**: 110108.
[26] He Y. Heat capacity, thermal conductivity, and thermal expansion of barium titanate-based ceramics. *Thermochim Acta* 2004, **419**: 135–141.
[27] Radhika Rao MV, Umarji AM. Thermal expansion studies on ferroelectric materials. *B Mater Sci* 1997, **20**: 1023–1028.
[28] Huang X, Zeng JT, Ruan XZ, *et al.* Structure, electrical, and thermal expansion properties of PZnTe–PZT ternary system piezoelectric ceramics. *J Am Ceram Soc* 2018, **101**: 274–282.
[29] Kim SJ, Kim YS. State dependent pyroelectric and thermal expansion coefficients in a PZT wafer. *Ceram Int* 2010, **36**: 2189–2196.
[30] Xu PH, Zhang XZ, Liu GW, *et al.* Microstructure and mechanical properties of SiC joint brazed by Al–Ti alloys as filler metal. *J Inorg Mater* 2022, **37**: 683–690.
[31] He YM, Zhang J, Liu CF, *et al.* Microstructure and mechanical properties of Si_3N_4/Si_3N_4 joint brazed with Ag–Cu–Ti + SiCp composite filler. *Mater Sci Eng A* 2010, **527**: 2819–2825.
[32] Wang B, Xu SC, Jin F, *et al.* Effect of $LiAlSiO_4$ particle size on the properties of LAS/SiC porous ceramics with near zero thermal expansion. *Ceram Int* 2014, **40**: 2853–2856.
[33] Cheng L, Liu SH, Jiang BW, *et al.* A review on the wettability and residual stress of AMB AlN/metal joints. *Mat Sci Semicon Proc* 2024, **174**: 108181.
[34] Amra M, Alavi Zaree SR, Dehmolaei R. Dissimilar welding between 1.4742 ferritic and 310S austenitic stainless steels: Assessment of oxidation behaviour. *Met Mater Int* 2021, **27**: 931–945.
[35] Mahapatra MK, Lu K. Sealing evaluation of an alkaline earth silicate glass for solid oxide fuel/electrolyser cells. *Fuel Cells* 2011, **11**: 436–444.
[36] Xiao JH, Zhang WY, Xiong CY, *et al.* Oxidation behavior of Cu-doped $MnCo_2O_4$ spinel coating on ferritic stainless steels for solid oxide fuel cell interconnects. *Int J Hydrogen Energ* 2016, **41**: 9611–9618.
[37] Wu XF, Zhu WB, He Y. Deformation prediction and experimental study of 316L stainless steel thin-walled parts processed by additive-subtractive hybrid manufacturing. *Materials* 2021, **14**: 5582.
[38] Dourandish M, Simchi A, Tamjid Shabestary E, *et al.* Pressureless sintering of 3Y–TZP/stainless-steel composite layers. *J Am Ceram Soc* 2008, **91**: 3493–3503.
[39] Kwabena Adomako N, Kim SH, Yoon JH, *et al.* Finite element modeling of residual stress at joint interface of titanium alloy and 17-4PH stainless steel. *Metals* 2021, **11**: 629.
[40] FR WM, Yoon DH, Raju K, *et al.* Interfacial microstructure and shear strength of reactive air brazed oxygen transport membrane ceramic–metal alloy joints. *Met Mater Int* 2018, **24**: 157–169.
[41] Nesbitt JA, Draper SL, Barrett CA. Cyclic oxidation of FeCrAlY/Al_2O_3 composites. *Mater High Temp* 2000, **17**: 139–147.
[42] Wang PC, Liu XF, Wang HH, *et al.* Negative thermal expansion $Y_2Mo_3O_{12}$ particles reinforced AgCuTi composite filler for brazing C_f/SiC and GH3536. *Mater Charact* 2022, **185**: 111754.
[43] Wang P, Liu X, Wang H, *et al.* Releasing the residual stress of C_f/SiC-GH3536 joint by designing an Ag–Cu–Ti + $Sc_2(WO_4)_3$ composite filler metal. *J Mater Sci Technol* 2022, **108**: 102–109.
[44] Ba J, Zheng XH, Ning R, *et al.* C/SiC composite–Ti_6Al_4V joints brazed with negative thermal expansion ZrP_2WO_{12} nanoparticle reinforced AgCu alloy. *J Eur Ceram Soc* 2019, **39**: 755–761.
[45] Zhou YH, Liu D, Niu HW, *et al.* Vacuum brazing of C/C composite to TC4 alloy using nano-Al_2O_3 strengthened AgCuTi composite filler. *Mater Design* 2016, **93**: 347–356.
[46] Meier AM, Chidambaram PR, Edwards GR. A comparison of the wettability of copper–copper oxide and silver–copper oxide on polycrystalline alumina. *J Mater Sci* 1995, **30**: 4781–4786.
[47] Singh M, Asthana R. Joining of ZrB_2-based ultra-high-temperature ceramic composites to Cu–clad–molybdenum for advanced aerospace applications. *Int J Appl Ceram Tec* 2009, **6**: 113–133.
[48] Durussel P, Feschotte P. A revision of the binary system Ag–Pt. *J Alloy Compd* 1996, **239**: 226–230.
[49] Si XQ, Cao J, Talic B, *et al.* A novel Ag based sealant for solid oxide cells with a fully tunable thermal expansion. *J Alloy Compd* 2020, **831**: 154608.
[50] Ishiguro T, Ishizawa N, Mizutani N, *et al.* High temperature structural investigation of the delafossite type compound $CuAlO_2$. *J Solid State Chem* 1982, **41**: 132–137.
[51] Roy R, Agrawal DK, McKinstry HA. Very low thermal expansion coefficient materials. *Annu Rev Mater Res* 1989, **19**: 59–81.

[52] Meng XL, Xiao B, Wu HH. Effects of Ti containing Cu-based alloy on sintering mechanism, element diffusion behavior and physical properties of glass–ceramic bond for cubic boron nitride abrasive tool materials. *Micromachines* 2023, **14**: 303.
[53] Habel D, Görke O, Tovar M, *et al.* Microstraining in titania-, alumina- and silica-supported V_2O_5-catalysts. *J Eur Ceram Soc* 2009, **29**: 1093–1099.
[54] Qiang LY, Zhang XZ, Jiang YH, *et al.* Sinterability, microstructure, thermal expansion behavior and mechanical properties of Nb_2O_5 ceramics. *China Ceram* 2021, **11**: 24–31. (in Chinese)
[55] Koh JH, Sorge E, Wen TC, *et al.* Thermal expansion behaviors of yttrium tungstates in the WO_3–Y_2O_3 system. *Ceram Int* 2013, **39**: 8421–8427.
[56] Rosen C, Banks E, Post B. The thermal expansion and phase transitions of WO_3. *Acta Crystallogr* 1956, **9**: 475–476.
[57] Dzhafarov TD, Altunbas M, Görür O. The high-temperature thermal expansion of BiPbSrCaCuO superconductor and the oxide components (Bi_2O_3, PbO, CaO, CuO). *J Mater Sci* 1996, **31**: 2207–2212.
[58] Lumpp JK, Chen N, Goretta KC. Mechanical properties of CuO. *High Temp Mat Pr-Isr* 1990, **9**: 1–6.
[59] Hu YM, Liu XS, Xu S, *et al.* Improving the thermal expansion and capacitance properties of MoO_3 by introducing oxygen vacancies. *J Phys Chem C* 2021, **125**: 10817–10823.
[60] Wong CP, Bollampally RS. Thermal conductivity, elastic modulus, and coefficient of thermal expansion of polymer composites filled with ceramic particles for electronic packaging. *J Appl Polym Sci* 1999, **74**: 3396–3403.
[61] Si XQ, Cao J, Ritucci I, *et al.* Enhancing the long-term stability of Ag based seals for solid oxide fuel/electrolysis applications by simple interconnect aluminization. *Int J Hydrogen Energ* 2019, **44**: 3063–3074.
[62] Si XQ, Cao J, Song XG, *et al.* Reactive air brazing of YSZ ceramic with novel Al_2O_3 nanoparticles reinforced Ag–CuO–Al_2O_3 composite filler: Microstructure and joint properties. *Mater Design* 2017, **114**: 176–184.
[63] Wang ZM, Yang JH, Qi FG, *et al.* Interfacial characterization and mechanical properties of reactive air brazed ZrO_2 ceramic joints with Ag–CuO–Al_2TiO_5 composite filler metal. *Ceram Int* 2021, **47**: 29128–29138.
[64] Kuterbekov KA, Nikonov AV, Bekmyrza KZ, *et al.* Classification of solid oxide fuel cells. *Nanomaterials* 2022, **12**: 1059.
[65] Shao ZB, Liu KR, Liu LQ, *et al.* Equilibrium phase diagrams in the systems PbO–Ag and CuO–Ag. *J Am Ceram Soc* 1993, **76**: 2663–2664.
[66] Weil KS, Kim JY, Hardy JS. Reactive air brazing: A novel method of sealing SOFCs and other solid-state electrochemical devices. *Electrochem Solid-ST* 2005, **8**: A133–A136.
[67] Kim JY, Hardy JS, Weil KS. Silver-copper oxide based reactive air braze for joining yttria-stabilized zirconia. *J Mater Res* 2005, **20**: 636–643.
[68] Bobzin K, Schlaefer T, Zhao LD, *et al.* Brazing of ceramic-to-ceramic and ceramic-to-metal joints in air. *Front Mech Eng China* 2010, **5**: 125–129.
[69] Sinnamon KE, Meier AM, Joshi VV. Wetting and mechanical performance of zirconia brazed with silver/copper oxide and silver/vanadium oxide alloys. *Adv Eng Mater* 2014, **16**: 1482–1489.
[70] Cao J, Si XQ, Li WJ, *et al.* Reactive air brazing of YSZ-electrolyte and Al_2O_3-substrate for gas sensor sealing: Interfacial microstructure and mechanical properties. *Int J Hydrogen Energ* 2017, **42**: 10683–10694.
[71] Si XQ, Cao J, Song XG, *et al.* Evolution behavior of Al_2O_3 nanoparticles reinforcements during reactive air brazing and its role in improving the joint strength. *Mater Design* 2017, **132**: 96–104.
[72] Si XQ, Wang D, Li C, *et al.* Exploring the role of Mn–Co spinel coating on Crofer 22 APU in adjusting reactions with the Ag based sealant during reactive air brazing. *J Mater Res Technol* 2022, **16**: 608–618.
[73] Phongpreecha T, Nicholas JD, Bieler TR, *et al.* Computational design of metal oxides to enhance the wetting and adhesion of silver-based brazes on yttria-stabilized-zirconia. *Acta Mater* 2018, **152**: 229–238.
[74] Hardy JS, Weil KS. Development of high-temperature air braze filler metals for use in two-step joining and sealing processes. *Weld J* 2008, **87**: 195–201.
[75] Chen L, Li C, Si XQ, *et al.* A novel Ag–$CuAlO_2$ sealant for reactive air brazing of 3YSZ and AISI 310S. *Ceram Int* 2021, **47**: 31413–31422.
[76] Wang ZQ, Li C, Kiebach R, *et al.* Joining of Co coated ferritic stainless steel to ceramic solid oxide cells by a novel Ag–SiO_2 braze. *J Mater Sci Technol* 2022, **121**: 174–180.
[77] Weil K S, Coyle CA, Darsell JT, *et al.* Effects of thermal cycling and thermal aging on the hermeticity and strength of silver–copper oxide air-brazed seals. *J Power Sources* 2005, **152**: 97–104.
[78] Kim JY, Hardy JS, Weil KS. Novel metal-ceramic joining for planar SOFCs. *J Electrochem Soc* 2005, **152**: J52–J58.
[79] Darsell JT, Weil KS. Effect of filler metal composition on the strength of yttria stabilized zirconia joints zrazed with Pd-Ag-CuO_x. *Metall Mater Trans A* 2008, **39A**: 2095–2105.
[80] Darsell JT, Weil KS. High temperature strength of YSZ joints brazed with palladium silver copper oxide filler metals. *Int J Hydrogen Energ* 2011, **36**: 4519–4524.
[81] Kuhn BJ, Wetzel FJ, Steinbrech RW, *et al.* Mechanical characterization of brazed ceramic/metal joints for SOFC stacks. In: Proceedings of the 8th European SOFC Forum, 2008
[82] Skiera E, Brandenberg J, Li CC, *et al.* Mechanical properties of reactive air brazed (RAB) metal/ceramic joints. Part 1: Visco-plastic deformation of silver-based reactive air brazes. *Adv Eng Mater* 2014, **16**: 1462–1467.
[83] Kuhn B, Wetzel FJ, Malzbender J, *et al.* Mechanical performance of reactive-air-brazed (RAB) ceramic/metal joints for solid oxide fuel cells at ambient temperature. *J Power Sources* 2009, **193**: 199–202.
[84] Kuhn B, Wessel E, Malzbender J, *et al.* Effect of isothermal aging on the mechanical performance of brazed ceramic/metal joints for planar SOFC-stacks. *Int J Hydrogen Energ* 2010, **35**: 9158–9165.
[85] Li CC, Kuhn B, Brandenberg J, *et al.* Improving contour accuracy and strength of reactive air brazed (RAB) ceramic/metal joints by controlling interface microstructure. *Adv Eng Mater* 2012, **14**: 394–399.
[86] Skiera E, Brandenberg J, Li CC, *et al.* Mechanical properties of reactive air brazed (RAB) metal/ceramic joints. Part 2: Tailored microstructure for thermal cycling resistance. *Adv Eng Mater* 2014, **16**: 1423–1429.
[87] Tillmann W, Sievers N, Pfeiffer J, *et al.* Examination of the porosity in reactive air brazed joints by ultrasonic testing. *Adv Eng Mater* 2014, **16**: 1437–1441.
[88] Pönicke A, Schilm J, Kusnezoff M, *et al.* Aging behavior of reactive air brazed seals for SOFC. *Fuel Cells* 2015, **15**: 735–741.
[89] Wang ZQ, Li C, Si XQ, *et al.* Brazing YSZ ceramics by a novel SiO_2 nanoparticles modified Ag filler. *Ceram Int* 2020, **46**: 16493–16501.
[90] Cao J, Wang ZQ, Li C, *et al.* Microstructure evolution and mechanical properties of Co coated AISI 441 ferritic stainless steel/YSZ reactive air brazed joint. *Int J Hydrogen Energ* 2021, **46**: 8758–8766.
[91] Yan YT, Liu BS, Xu TX, *et al.* Realizing the air brazing of ZrO_2 ceramics through Al metal. *J Materiomics* 2022, **8**: 662–668.
[92] Zhou WL, Hu SP, Yang MJ, *et al.* Reactive air brazing of 3YSZ ceramic to aluminized Crofer22H stainless steel using Ag–CuO fillers. *Int J Appl Ceram Tec* 2022, **19**: 2367–2378.
[93] Sun Z, Zhang LX, Li X, *et al.* Reactive air brazing of the YSZ/AISI 310s couples using a novel Ag–Nb_2O_5 sealant. *Ceram Int* 2020, **46**: 5168–5174.
[94] Yang J H, Yang Z W, Wang Y, *et al.* Interfacial microstructure and mechanical properties of reactive air brazed joints of ZrO_2 ceramic and GH3536. *Rare Metal Mat Eng* 2021, **50**: 4450–4456. (in Chinese)
[95] Liu GW, Zhang XZ, Yang J, *et al.* Recent advances in joining of SiC-

based materials (monolithic SiC and SiC_f/SiC composites): Joining processes, joint strength, and interfacial behavior. *J Adv Ceram* 2019, **8**: 19–38.

[96] Si XQ, Wang XY, Li C, *et al.* Joining 3YSZ electrolyte to AISI 441 interconnect using the Ag particle interlayer: Enhanced mechanical and aging properties. *Crystals* 2021, **11**: 1573.

[97] Si XQ, Li C, Zheng QW, *et al.* Reactive air brazing of SOFC using Ag–CuO–Al_2O_3 composite braze and the service performance study. *Trans China Weld Inst* 2020, **41**: 1–6. (in Chinese)

[98] Wang ZQ, Li C, Cao J, *et al.* Ag–SiO_2—An optimized braze for robust joining of commercial coated stainless steel to ceramic solid oxide cells. *Ceram Int* 2022, **48**: 32740–32747.

[99] Hardy JS, Kim JY, Weil KS. Joining mixed conducting oxides using an air-fired electrically conductive braze. *J Electrochem Soc* 2004, **151**: J43–J49.

[100] Weil KS, Kim JY, Hardy JS. Interfacial analysis of $(La_{0.6}Sr_{0.4})(Co_{0.2}Fe_{0.8})O_{3-\delta}$ substrates wetted by Ag–CuO. *J Mater Sci* 2005, **40**: 2341–2348.

[101] Hardy JS, Kim JY, Thomsen EC, *et al.* Improved wetting of mixed ionic/electronic conductors used in electrochemical devices with ternary air braze filler metals. *J Electrochem Soc* 2007, **154**: P32–P39.

[102] Chen H, Li LJ, Kemps R, *et al.* Reactive air brazing for sealing mixed ionic electronic conducting hollow fibre membranes. *Acta Mater* 2015, **88**: 74–82.

[103] Kaletsch A, Bezold A, Pfaff EM, *et al.* Effects of copper oxide content in AgCuO braze alloy on microstructure and mechanical properties of reactive-air-brazed $Ba_{0.5}Sr_{0.5}Co_{0.8}Fe_{0.2}O_{3-\delta}$ (BSCF). *J Ceram Sci Technol* 2012, **3**: 95–103.

[104] Joshi VV, Meier A, Darsell J, *et al.* Trends in wetting behavior for Ag–CuO braze alloys on $Ba_{0.5}Sr_{0.5}Co_{0.8}Fe_{0.2}O_{(3-\delta)}$ at elevated temperatures in air. *J Mater Sci* 2013, **48**: 7153–7161.

[105] Zhang YW, Zhang LL, Guo W, *et al.* Interfacial reaction and microstructural evolution of Ag–Cu braze on $BaCo_{0.7}Fe_{0.2}Nb_{0.1}O_{3-\delta}$ at high temperature in air. *Ceram Int* 2017, **43**: 810–819.

[106] Zhang YW, Liu T, Zhang JL, *et al.* Induction brazing $BaCo_{0.7}Fe_{0.2}Nb_{0.1}O_{3-\delta}$ membrane tubes to steel supports with Ag-based filler in air. *J Membrane Sci* 2017, **533**: 19–27.

[107] Zhang C, Lv JJ, Bai D, *et al.* Wetting transition behavior of Ag–Cu alloy braze on $BaCo_{0.7}Fe_{0.2}Nb_{0.1}O_{3-\delta}$ ceramic. *Ceram Int* 2021, **47**: 14427–14437.

[108] Si XQ, Su Y, Li C, *et al.* Reactive air brazing of $BaCe_{0.7}Zr_{0.1}Y_{0.1}Yb_{0.1}O_{3-\delta}$ proton conductive ceramic and stainless steel. *Trans China Weld Inst* 2022, **43**: 8–14. (in Chinese)

[109] Wang XY, Si XQ, Li C, *et al.* Joining the $BaZr_{0.1}Ce_{0.7}Y_{0.1}Yb_{0.1}O_{3-\delta}$ electrolyte to AISI 441 interconnect for protonic ceramic fuel cell applications: Interfacial microstructure and long-term stability. *ACS Appl Energy Mater* 2021, **4**: 7346–7354.

[110] Zhang LL, Li K, Yu CC, *et al.* Wetting properties and interface reaction mechanism of Ag–Cu brazes on dual-phase membrane ceramic. *J Inorg Mater* 2016, **31**: 607–612.

[111] Sydorenko TV, Naidich YV. Wettability by liquid metals, metallization and brazing of barium titanate ceramics. *Weld J* 2014, **93**: 6s–14s.

[112] Canu G, Valenza F. Effect of Zr content on the wetting of $BaTi_{1-x}Zr_xO_3$ perovskite ceramics by Ag-based liquids. *J Eur Ceram Soc* 2022, **42**: 3886–3891.

[113] Pavlina EJ, Meier AM, Monteleone P, *et al.* Development of silver–metal oxide reactive air braze alloys for electroding PZT ceramics. *J Mater Sci* 2007, **42**: 705–713.

[114] Kaletsch A, Pfaff EM, Broeckmann C. Effect of aging on microstructure and mechanical strength of reactive air brazed BSCF/AISI 314-joints. *Adv Eng Mater* 2014, **16**: 1430–1436.

[115] Herzog S, Kaletsch A, Broeckmann C. Reduced strength degradation of reactive air brazed $Ba_{0.5}Sr_{0.5}Co_{0.8}Fe_{0.2}O_{3-\delta}$ membranes by pre-oxidation of metallic components. *Mater Sci Eng A* 2022, **857**: 143993.

[116] Herzog S, Kaletsch A, Broeckmann C. Diffusion barriers minimizing the strength degradation of reactive air brazed $Ba_{0.5}Sr_{0.5}Co_{0.8}Fe_{0.2}O_{3-\delta}$ membranes during aging. *Membranes* 2023, **13**: 504.

[117] Herzog S, Boussinot G, Kaletsch A, *et al.* Microstructure coarsening in $Ba_{0.5}Sr_{0.5}Co_{0.8}Fe_{0.2}O_{3-\delta}$ during reactive air brazing. *J Eur Ceram Soc* 2022, **42**: 5842–5850.

[118] Rudenskiy D, Herzog S, Horbach L, *et al.* Numerical modeling of residual stresses and fracture strengths of $Ba_{0.5}Sr_{0.5}Co_{0.8}Fe_{0.2}O_{3-\delta}$ in reactive air brazed joints. *Materials* 2023, **16**: 7265.

[119] Zhang JL, Zhang J, Li LQ, *et al.* Stress analysis of the brazing joints of tubular ceramic oxygen-permeable membranes and metal supports. *Ceram Int* 2019, **45**: 1545–1553.

[120] Zhang C, Lv JJ, Chen ZY, *et al.* Microstructure evolution of Ag–Cu/$BaCo_{0.7}Fe_{0.2}Nb_{0.1}O_{3-\delta}$ joints in air and argon atmospheres. *J Asian Ceram Soc* 2021, **9**: 710–718.

[121] Wang XY, Si XQ, Gao JW, *et al.* Effects of the Mn–Co spinel coating on $BaZr_{0.1}Ce_{0.7}Y_{0.1}Yb_{0.1}O_{3-\delta}$/AISI 441 reactive air brazed joint: Microstructure, strength, and stability. *Ceram Int* 2023, **49**: 5154–5160.

[122] Raju K, Muksin, Yoon DH. Reactive air brazing of GDC–LSCF ceramics using Ag–10 wt% CuO paste for oxygen transport membrane applications. *Ceram Int* 2016, **42**: 16392–16395.

[123] Kim MD, Muhamad FR, Raju K, *et al.* Efficacy of Ag–CuO filler tape for the reactive air brazing of ceramic–metal joints. *J Korean Ceram Soc* 2018, **55**: 492–497.

[124] Raju K, Kim S, Seong YH, *et al.* Effects of reactive air brazing parameters on the interfacial microstructure and shear strength of GDC–LSM/Crofer 22 APU joints. *J Korean Ceram Soc* 2019, **56**: 394–398.

[125] Li YF, Xu YS, Yin YR, *et al.* Entropy engineering design of high-performing lithiated oxide cathodes for proton-conducting solid oxide fuel cells. *J Adv Ceram* 2023, **12**: 2017–2031.

[126] Wang LL, Wang L, Xu XY, *et al.* Research progress of bullet-resistant Al_2O_3 ceramics for protective armor. *Adv Ceram* 2023, **44**: 263–273. (in Chinese)

[127] Li M, Ai JP, Wang ZJ, *et al.* HPMA modified aluminium nitride powder for aqueous tape casting of AlN ceramic substrates. *J Adv Ceram* 2023, **12**: 1701–1711.

[128] Chen X, Yin J, Huang LZ, *et al.* Microstructural tailoring, mechanical and thermal properties of SiC composites fabricated by selective laser sintering and reactive melt infiltration. *J Adv Ceram* 2023, **12**: 830–847.

[129] Si XQ, Wang XY, Guo XJ, *et al.* Review of reactive air brazing: Fundamental, progress, and perspective. *Mater Design* 2024, **243**: 113073.

[130] Kim JY, Hardy JS, Wei KS. Dual-atmosphere tolerance of Ag–CuO-based air braze. *Int J Hydrogen Energ* 2007, **32**: 3655–3663.

[131] Kim JY, Engelhard M, Choi JP, *et al.* Effects of atmospheres on bonding characteristics of silver and alumina. *Int J Hydrogen Energ* 2008, **33**: 4001–4011.

[132] Chatzimichail R, Triantafyllou G, Tietz F, *et al.* Interfacial properties of (Ag + CuO) brazes used as sealing materials in SOFC stacks. *J Mater Sci* 2014, **49**: 300–313.

[133] Erskine KM, Meier AM, Joshi VV, *et al.* The effect of braze interlayer thickness on the mechanical strength of alumina brazed with Ag–CuO braze alloys. *Adv Eng Mater* 2014, **16**: 1442–1447.

[134] Prevost E, DeMarco AJ, MacMichael B, *et al.* Microstructural development and mechanical properties for reactive air brazing of ZTA to Ni alloys using Ag–CuO braze alloys. *Adv Eng Mater* 2014, **16**: 1448–1455.

[135] Wang TP, Sun MC, Li HQ, *et al.* Study on the microstructure of air reactive brazing joint between Al_2O_3 ceramic and Q235 steel. *J Phys Conf Ser* 2021, **2125**: 012071.

[136] Wang XY, Li C, Du Q, *et al.* Brazing ZTA ceramic and Ti_6Al_4V alloy directly in air: Excellent oxidation resistance at 800 °C. *Ceram*

Int 2022, **48**: 9631–9639.
[137] Kim JY, Hardy JS, Weil KS. Use of aluminum in air-brazing aluminum oxide. *J Mater Res* 2004, **19**: 1717–1722.
[138] Kim JY, Hardy JS, Weil KS. Ag–Al based air braze for high temperature electrochemical devices. *Int J Hydrogen Energ* 2007, **32**: 3754–3762.
[139] Kim JY, Choi JP, Weil KS. Mechanical properties and dual atmosphere tolerance of Ag–Al based braze. *Int J Hydrogen Energ* 2008, **33**: 3952–3961.
[140] Bobzin K, Kopp N, Wiesner S. Influence of filler and base material on the pore development during reactive air brazing. *Adv Eng Mater* 2014, **16**: 1456–1461.
[141] Wang ZQ, Li C, Si XQ, *et al.* Microstructure and mechanical properties of Al_2O_3 ceramic joints achieved by Ag–SiO_2 braze in air. *Int J Appl Ceram Tec* 2022, **19**: 508–513.
[142] Qiu YD, Xu SJ, Zhang XZ, *et al.* Reactive air wetting and brazing of Al_2O_3 ceramics using Ag–Nb_2O_5 filler: Performance and interfacial behavior. *J Adv Ceram* 2024, **13**: 135–142.
[143] Luo Y, Song XG, Hu SP, *et al.* Reactive air brazing of Al_2O_3 ceramic with Ag–CuO–Pt composite fillers: Microstructure and joint properties. *J Eur Ceram Soc* 2021, **41**: 1407–1414.
[144] Waetzig K, Schilm J, Mosch S, *et al.* Influence of the brazing paste composition on the wetting behavior of reactive air brazed metal–ceramic joints. *Adv Eng Mater* 2021, **23**: 2000711.
[145] Fernie JA, Drew RAL, Knowles KM. Joining of engineering ceramics. *Int Mater Rev* 2009, **54**: 283–331.
[146] Liu GW, Valenza F, Muolo ML, *et al.* SiC/SiC and SiC/Kovar joining by Ni–Si and Mo interlayers. *J Mater Sci* 2010, **45**: 4299–4307.
[147] Yan YT, Li PX, Zhang ZL, *et al.* Interfacial Si–O coordination for inhibiting the graphite phase enables superior SiC/Nb heterostructure joining by AuNi. *Compos Part B Eng* 2024, **282**: 111557.
[148] Liu WH, Wang PC, Shi WT, *et al.* Achieving ultrafine grain strengthening C_f/SiC-GH3536 joints brazed with Cu–Ti–WC composite interlayer via cold spray additive manufacturing. *Addit Manuf* 2024, **89**: 104258.
[149] Wang ZQ, Li C, Si XQ, *et al.* Interfacial microstructure and mechanical properties of SiC joints achieved by reactive air brazing using Ag–V_2O_5 filler. *J Eur Ceram Soc* 2019, **39**: 2617–2625.
[150] Wang RD, Zhang C, Li D, *et al.* Wettability and interfacial reaction mechanism between Ag–Cu alloy and Si_3N_4 ceramics in air atmosphere. *Ceram Int* 2021, **47**: 33078–33088.
[151] Luo Y, Hu SP, Li ZH, *et al.* Microstructure and properties of AlN ceramic reactive air brazing joints using Ag–CuO brazes. *J Mech Eng* 2020, **56**: 95–101. (in Chinese)
[152] Guo QH, Xu SJ, Zhang XZ, *et al.* Microstructures and interfacial behavior of Ag–CuO/AlN system by air wetting and brazing: Experiments and first-principles calculations. *J Eur Ceram Soc* 2024, **44**: 4963–4974.